Highlights

Melting conditions and mantle source composition from probabilistic joint inversion of major and rare earth element concentrations

B. Oliveira, J.C. Afonso, M. Klöcking

- Research highlight 1

- Research highlight 2

Melting conditions and mantle source composition from probabilistic joint inversion of major and rare earth element concentrations

B. Oliveira[a], J.C. Afonso[a,b], M. Klöcking[c]

[a]*Macquarie University, Department of Earth and Environmental Sciences, Sydney, NSW, 2109, Australia*
[b]*Centre for Earth Evolution and Dynamics, Department of Geosciences, University of Oslo*
[c]*The Australian National University, Research School of Earth Sciences, Canberra, ACT, 0200, Australia*

Abstract

The chemical composition of erupted basalts provides a record of the thermo-chemical state of their source region and the melting conditions that lead to their formation. Here we present the first probabilistic inversion framework capable of inverting both trace and major element data of mafic volcanic rocks to constrain mantle potential temperature, depth of melting, and major and trace element source composition. The inversion strategy is based on the combination of i) a two-phase multi-component reactive transport model, ii) a thermodynamic solver for the evolution of major elements and mineral/liquid phases, (iii) a disequilibrium model of trace element partitioning and iv) an adaptive Markov chain Monte Carlo algorithm. The mechanical and chemical evolution of melt and solid residue are therefore modelled in an internally- and thermodynamically-consistent manner.

We illustrate the inversion approach and its sensitivity to relevant model parameters with a series of numerical experiments with increasing level of

complexity. We show the benefits and limitations of using major and trace element compositions separately before demonstrating the advantages of a joint inversion. We show that such joint inversion has great sensitivity to mantle temperature, pressure range of melting and composition of the source, even when realistic uncertainties are assigned to both data and predictions. We further test the reliability of the approach on a real dataset from a well-characterised region: the Rio Grande Rift in western North America. We obtain estimates of mantle potential temperature (~ 1340 ^{o}C), lithospheric thickness (~ 60 km) and source composition that are in excellent agreement with numerous independent geochemical and geophysical estimates. In particular, this study suggests that the basalts in this region originated from a moderately hot upwelling and include the contribution from a slightly depleted source that experienced a small degree of melt or fluid metasomatism. This component is likely associated with partial melting of the lower portions of the lithosphere. The flexibility of both the melting model and inversion scheme developed here makes the approach widely applicable to assessing the thermo-chemical structure and evolution of the lithosphere-asthenosphere system and paves the way for truly joint geochemical-geophysical inversions.

2

1. Introduction

Most volcanism observed on Earth is the result of partial melting in the mantle. The compositions of these melts, as well as that of the residual mantle, carry valuable information on the composition of the source rock and on the pressure and temperature (P-T) conditions of melting (e.g. Hofmann and Feigenson, 1983; Michard and Albarède, 1986; Richter, 1986; Navon and Stolper, 1987; McKenzie and O'Nions, 1991; Feigenson et al., 1996; Zou, 1997). One of the simplest approaches to extract this information is the analysis and modelling of the trace element contents of primitive melts and their residues (e.g. Gast, 1968; Minster and Allègre, 1978; Albarède, 1983; McKenzie and O'Nions, 1991; Liu and Liang, 2017; Brown et al., 2020; Zou, 1997). This is mainly due to: i) trace elements are highly sensitive to specific aspects of the melting process; ii) their modelling is simple, as they can be assumed to behave as solutes in *ideal* solutions; and iii) their compositional range is not as restricted or interdependent as that of major elements. In contrast, the chemical behaviour of major elements during melting is substantially more complicated to model, requiring sophisticated empirical parameterizations or, preferably, full thermodynamic modelling. Despite these complexities, it is clearly desirable to be able to include both major and trace element information into melting models, as they carry important and complementary information on melting conditions and regimes. For instance, trace elements offer invaluable information on melting processes resulting from low-degree partial melting, something major elements are not very sensitive to. However, when the degree of melting is large or our interest is the thermodynamics of magmatic processes, major elements become more infor-

3

mative. Furthermore, major element distributions influence the mineralogy of the source rock during melting, which in turn controls trace element partitioning. Perhaps more importantly, the characterization of both melts and residues in terms of major elements allows us to predict lithologies and their bulk physical properties (e.g. density, seismic velocity, electrical conductivity), which paves the way for joint studies of the upper mantle that combine geochemical, geophysical and/or geodynamic techniques.

There are two main approaches for interpreting compositional data in terms of melting conditions: *forward* and *inverse* modelling. In the forward approach, a specific model of mantle melting is devised and used to make predictions of a number of relevant rock properties, such as bulk composition or mineral assemblage. By comparing these model predictions with observed values, the validity of the melting model and its fundamental assumptions are assessed in a trial-and-error manner. In the inverse approach, a quantitative assessment of the likelihood of the melting model and the parameters controlling its predictions is performed according to their ability to explain the observed data. An error (or cost) function that measures the discrepancies between model predictions and observations is formally defined and used by an algorithm to guide the inversion towards optimal models in terms of their data-fit characteristics. In the so-called *deterministic* inversions, the error function is minimised to obtain a single best-fitting or optimal model. This is the strategy followed, for instance, in the classic works of Minster and Allègre (1978), Albarède (1983), and McKenzie and O'Nions (1991). In contrast, *probabilistic* inversions (also known as *statistical* or *Bayesian*) consider the model parameters to be random variables described by probabil-

ity distributions (Kaipio and Somersalo, 2005; Tarantola, 2005). Rather than producing a single best-fitting model, the task of a probabilistic inversion is to obtain a complete probability distribution over the parameters of interest by combining observations and available prior information. This distribution is referred to as the *posterior* distribution and constitutes the most general solution to an inverse problem.

While probabilistic inversions have been popular in geophysics for over three decades, only a few recent studies have applied them in the context of mantle melting (e.g. Liu and Liang, 2017; Kimura, 2017; Brown et al., 2020). In particular, thermodynamically-constrained disequilibrium treatments of both major and trace elements in melts and residues have not yet been attempted. Perhaps more importantly, comprehensive assessments of both data and model uncertainties, and their impact on interpretations regarding the nature of melting in the mantle, remain largely unexplored. Yet, this information is crucial to assessing the validity of interpretations and assumptions about melting in the mantle, as well as to devise new techniques to reduce uncertainty in our interpretations.

In this paper, we present a new approach that combines a thermodynamically-constrained disequilibrium model of mantle melting with a probabilistic inversion scheme. We use this approach to explore the individual and joint sensitivity of major and trace elements in basaltic rocks to i) the pressure and temperature conditions of melting and ii) trace and major element composition of the source, accounting for both data and model uncertainties. In what follows, we first describe the melting model and briefly explore its general behaviour in terms of predicted trace and major element composi-

tions of melts and residues. We then outline the Bayesian strategy adopted to invert trace and major element compositions of primitive volcanic rocks for melting conditions and source composition. We illustrate the benefits and limitations of our approach with a set of representative numerical examples. We further test the approach on a well-studied real data set from the Rio Grande Rift, where abundant independent information is available on the thermo-chemical structure of the upper mantle. We show that this new modelling approach has important implications for the quantitative assessment of upper mantle processes and opens up the possibility of joint geochemical-geophysical inversions for the thermo-chemical structure and evolution of the lithosphere-asthenosphere system.

2. Melting model

2.1. Background on melting models

Often quantitative and predictive frameworks for mantle melting are based on (i) a melting function, (ii) a chemistry function and (iii) a mixing function (e.g. Langmuir et al., 1992; Plank and Langmuir, 1992; Asimow, 2001; Brown and Lesher, 2016). The melting function describes the amount of melt generated per increment of pressure, known as polybaric productivity dF/dP, and is typically either assumed to be constant (e.g. Klein and Langmuir, 1987; Niu and Batiza, 1991) or approximated via empirical functions based on parameterizations of melting experiments (e.g. Katz et al., 2003). The chemistry function specifies the chemical compositions of the melt and the solid residue as a function of degree of melting, F. For the case of trace-elements, this is commonly done using experimentally-constrained partition

6

coefficients. Lastly, the role of the mixing function is to describe the spatial distribution of both solid and melt within the melting regime, including how instantaneous melts within the melting zone are aggregated and extracted.

Despite often being constructed separately, previous works demonstrate that these three functions are intimately related to one another (e.g. Langmuir et al., 1992; Plank and Langmuir, 1992; Asimow, 2001; Smith and Asimow, 2005; Tirone et al., 2009; Rudge et al., 2011; Oliveira et al., 2017; Keller and Katz, 2016). For instance, the melting and chemistry functions must satisfy mass and energy balance constraints, as they are both controlled by the same thermodynamic principles. Furthermore, the chemical compositions of both melt and solid depend on the chemical reactions occurring along their individual trajectories during the melting process. As a consequence, the melting and chemistry functions are tightly coupled to the mixing function.

Following previous studies such as that of Asimow (2002), we propose an internally-consistent thermodynamic framework for decompression melting in a one-dimensional upwelling mantle column (Fig. 1). We assume an isentropic fractional fusion model, which in practice is modelled as a sequence of infinitesimal isentropic melting steps along the melting column. At each step, the newly produced melt (Fig. 1, blue lines) is extracted and isolated into an adjacent melt reservoir (Fig. 1, red lines). In order to capture relative movement between solid and melt phases during the melting process, we couple the internally-consistent thermodynamic database and formalism for mantle melting of Jennings and Holland (2015) with a two-phase transport model. As such, we integrate the melting, chemistry and mixing functions into a single thermo-chemical-dynamical framework. We use components of

the software Perple_X (Connolly, 2009) to obtain degree of melting as a function of pressure, temperature and bulk composition (i.e. melting function) via Gibbs free-energy minimization. This also allows us to obtain the major element compositions of both solids and melts, as well as the mineral assemblage within the solid residue. The latter is then used to calculate trace-element compositions of solids and melts in an additional "chemistry function", that includes trace-element diffusion within mineral grains and differential flow between melts and the solid matrix. Because of the strong sensitivity of trace-element fractionation to changes in the mineral assemblage, this approach is particularly well suited for integrated interpretations of major and trace element signatures in volcanic rocks and residual mineral phases (e.g. Smith and Asimow, 2005).

Finally, we use the "residual mantle column" approach (Plank and Langmuir, 1992) to evaluate the geochemical effects of mantle flow on the average melt compositions obtained by the melting model. This approach enables the use of simplified one-dimensional melting models to approximate melt aggregation and mixing in more complex tectonic settings with two- or three-dimensional mantle flow. The shape of the residual mantle column is a function of the rate at which the solid residue exits the melting zone at any given depth (Plank and Langmuir, 1992), and is used to compute the relative depth-dependent weighting of instantaneous melts within the final aggregated melt. For instance, in the end-member case of passive upwelling, the solid residue exits the melting zone at the same velocity at all depths. Therefore, the mean melt composition is computed by pooling all melts extracted from different depths along the melting column (Ito and Mahoney,

2005). Other mantle flow regimes produce different shapes of the residual mantle column, leading to different depth-dependent weighting of melts, and thus, different estimations of mean melt properties. A complete derivation of the melting model, and a list of the main variables used in this study can be found in Appendix A.

2.2. Melting function

In practice, we model fractional fusion as a series of isentropic decompression melting steps in equilibrium, each followed by complete chemical isolation of major elements in the liquid phase from the residual solid. Instead of using empirical parameterizations for mantle melting (e.g. for solidus and liquidus temperatures, isobaric productivity, latent heat of melting), our approach rests on an internally-consistent thermodynamic model for the liquid and solid phases in mantle peridotites (Jennings and Holland, 2015). Given pressure, temperature and solid composition at each incremental depth z_i, we minimise Gibbs free-energy using Perple_X to obtain solid and melt equilibrium compositions, thermodynamic properties and the equilibrium mineral assemblage. If melting is isentropic, the associated temperature change between two consecutive decompression steps is not a free variable and is not known *a priori*. This problem can be circumvented by either estimating this temperature change using thermodynamic constraints or by minimizing a thermodynamic potential such as enthalpy to guarantee isentropic conditions at each incremental depth (Asimow et al., 1997; Morgan, 2001; Brown and Lesher, 2016). Since we rely on a Gibbs free-energy minimization algorithm, we opt to correct the temperature iteratively at each pressure increment until the difference between the entropy of the system before and after each mini-

mization falls below a certain tolerance. Once the temperature of the system corresponds to that of an isentropic decompression melting step, the melt fraction and its entropy are removed from the system (which does not affect the specific entropy of the solid residue, nor its composition). We record solid and melt compositions and thermodynamic properties, and proceed with the next isentropic decompression melting step.

At every decompression step, we calculate $F(z_i)$ by adding the extracted melt mass fraction to the degree of melting obtained in the previous decompression melting step $F(z_{i-1})$ as

$$F(z_i) = F(z_{i-1}) + (1 - F(z_{i-1})) f(z_i) \tag{1}$$

where f refers to the generated melt mass fraction in equilibrium. Similarly, for each mineral phase we define

$$F_j(z_i) = F_j(z_{i-1}) + (1 - F(z_{i-1})) f_j(z_i) \tag{2}$$

where f_j is the mass fraction of mineral phase j. F_j describes the mass change of each mineral phase as a result of phase transformations, including solid-solid phase transitions. Unlike the degree of melting F, F_j can decrease in a decompression step.

2.3. Chemistry function

The major-element compositions of both solid and instantaneous melt at each decompression step are directly retrieved from the energy minimization algorithm (Perple_X), assuming local thermodynamic equilibrium. In contrast, trace element partitioning between instantaneous melts and solid

residues results from phase-change effects and diffusive flux within mineral grains (Liang and Liu, 2016; Oliveira et al., 2020, and Appendix A). The rate of chemical equilibration of trace elements is therefore controlled by diffusion of chemical species in the mineral grains.

According to the model presented in Appendix A, the trace element composition of instantaneous melts (i.e. newly formed instantaneous melts, c_{inst}^b), isolated melts (i.e. chemically isolated melts, c_{iso}^b) and mineral phases (c_j^b) along a one-dimensional column read

$$\phi_{inst}\rho_{inst}w\frac{d}{dz}c_{inst}^b = \Gamma^b - c_{inst}^b\Gamma \tag{3}$$

$$\phi_{iso}\rho_{iso}w\frac{d}{dz}c_{iso}^b = \left(c_{inst}^b - c_{iso}^b\right)S \tag{4}$$

$$\phi_j\rho_jW\frac{d}{dz}c_j^b = -\Gamma_j^b + c_j^b\Gamma_j \tag{5}$$

where ϕ is volume fraction (subscripts $inst$, iso, s and j refer to instantaneous liquid, isolated liquid, solid and mineral phases, respectively), ρ is density, z is depth, and w and W are the liquid and solid velocities. Γ corresponds to the mass-transfer from solid to instantaneous melts, and S is the mass-transfer from the instantaneous melts to the isolated melt. Since the total solid mass corresponds to that of all individual mineral phases, we have $c_s^b = \sum_j \phi_j\rho_j c_j^b$. The total mass-transfer rate is $\Gamma = \sum_j \Gamma_j$ and $\Gamma^b = \sum_j \Gamma_j^b$.

Here, instantaneous melts are kept in chemical isolation upon formation, which implies that $\phi_{inst} = 0$, $S = \Gamma$, and that the total melt fraction is equal to the melt in chemical isolation, $\phi_l = \phi_{iso}$. With these considerations we simplify Eqs. 3 and 4 and obtain

11

$$c_{inst}^b = \frac{\Gamma^b}{\Gamma} \tag{6}$$

$$\phi_l \rho_l w \frac{d}{dz} c_{iso}^b = \left(c_{inst}^b - c_{iso}^b \right) \Gamma \tag{7}$$

The mass-transfer term of chemical component b, Γ_j^b, considers both phase changes and diffusion of trace elements from mineral phases to melt as

$$\Gamma_j^b = c_j^b \Gamma_j + \phi_j \rho_j R_j^b \left(c_j^b - K_j^b c_{inst}^b \right) \tag{8}$$

where R_j^b is the diffusion-dependent exchange rate constant for the chemical component b between mineral j and the instantaneous liquid (see Appendix A for further details). K_j^b refers to the partition coefficient for chemical component b between mineral phase j and the liquid. According to Eq. 8, chemical compositions in mineral phases and instantaneous melts will completely equilibrate only if $R_j^b \to \infty$ (i.e. $c_j^b = K_j^b c_{inst}^b$).

Finally, we complete the chemistry function with a two-phase flow model for the solution of melt fraction and velocities of both solid and melts (cf. McKenzie, 1984; Oliveira et al., 2017). As shown in Appendix A, the fluxes of liquid, solid, and mineral phases along a one-dimensional steady-state melting column are

$$\phi_l \rho_l w = \int_0^h \Gamma \tag{9}$$

$$\phi_j \rho_j W = - \int_0^h \Gamma_j \tag{10}$$

12

where "0" refers to properties evaluated at the onset of melting, and h is the depth at which melting stops. In steady-state, the mass-transfer rate Γ is related to the degree of melting F obtained from the melting function via $F(z) = \int_0^h \Gamma dz / \rho_s^0 W^0$, and similarly $F_j(z) = \int_0^h \Gamma_j dz / \rho_s^0 W^0$. With this information we rewrite Eqs. 9–10 and obtain

$$\phi_l \rho_l w = \rho_s^0 W_0 F \tag{11}$$

$$\phi_j \rho_j W = \rho_s^0 W_0 \left(\frac{\phi_j^0 \rho_j^0}{\rho_s^0} - F_j \right) \tag{12}$$

Equations 11 and 12 show that the liquid and solid fluxes (i.e. products of volume fraction, density and velocity) are balanced by melt production. Therefore, once the liquid volume fraction is known, solid and liquid velocities can be determined. Equation 11 is used to obtain the liquid fraction.

We relate ϕ_l, w and W with a Darcy-type functional relationship

$$0 = \frac{\mu_l}{k_0 \phi^{n-1}} (W - w) + (1 - \phi_l) (\rho_s - \rho_l) \mathbf{g} \tag{13}$$

where μ_l is the liquid viscosity, k_0 is the permeability constant, n the permeability exponent, and $\mathbf{g}$ is the acceleration of gravity. Equation 13 shows that melt segregation is governed by a balance between the differential buoyancy of the melt and the resistance to flow of melt through the matrix (Darcy resistance). For simplicity, we ignore the resistance of the solid phase to deformation which is of second-order only (no compaction term in Eq. 13).

13

2.4. Mixing function

Since we assume a one-dimensional upwelling model, further assumptions are needed to capture the effects of lateral mantle flow on the modelled compositions. Given its applicability to a wide range of tectonic settings, we employ the "residual mantle column" approach to approximate the pooling of melts over the whole melting zone (Plank and Langmuir, 1992).

Given our model assumptions, the average major and trace element concentrations of the pooled magma can be calculated as

$$c_{ave}^b = \frac{\int_0^h FU c_{iso}^b dz}{\int_0^h FU dz} \qquad (14)$$

where U refers to the normalised speed at which the solid residue exits the melting zone (Ito and Mahoney, 2005). U acts as a weighting factor ($0 \leq U \leq 1$) that accounts for the contribution of melts from different depths to the total volume of pooled melt extracted from the melting zone. In order to derive appropriate functionals for U, the mantle dynamics within the melting zone for each tectonic setting need to be examined. For instance, during passive upwelling at a mid-ocean ridge, where mantle flow is driven kinematically by two diverging plates, horizontal flow is nearly uniform with depth and $U = 1$ (McKenzie and O'Nions, 1991). During active upwelling, however, lateral transport might be considered negligible and U is zero everywhere except at the top boundary. Hybrid models of mantle flow combining passive and active upwelling contributions can also be captured with Eq. 14 (e.g. Plank and Langmuir, 1992; Ito and Mahoney, 2005).

Note that the definition of the mixing function in Eq. 14 is not unique, and it is a direct consequence of the assumed melting model. Instead of

using a "residual mantle column" approach, other authors incorporate the heterogeneous modes of transport in their melting model (e.g. Keller et al., 2017). Therefore, their modelled compositions are already the result of integrated reaction and transport rates along the solid and melt trajectories through pressure-temperature space (P-T), and thus no further mixing function is required (or a different one). However, application of such models within an inversion scheme have remained elusive due to their relatively high computational cost.

2.5. Behaviour of the system

Here we describe the general behaviour of the melting model in response to different parameter choices. Figure 2 shows a range of solutions obtained by systematically varying the permeability constant, k_0, and the upwelling velocity at the onset of melting, W_0. As demonstrated elsewhere (Ribe, 1985; Asimow and Stolper, 1999), temperature, degree of melting (F) and the individual chemical compositions of solid phases and liquids are independent of the flow parameters in a thermally and chemically equilibrated, one-dimensional, steady-state melting column (Figs. 2a,b,f,g). Since P-T and the individual chemical compositions are the same, phase proportions also remain unchanged (Fig. 2e,j). This is not the case, however, for melt fraction, ϕ_l, and velocity contrasts between melt and matrix, Δv. Large k_0 values imply higher permeabilities, which results in more efficient melt extraction and higher melt velocities (Eq. 13 and Fig. 2.e). On the contrary, small values of k_0 result in melts travelling at a similar velocity as that of their host matrix (i.e. $\Delta v \approx 0$, Fig. 2.d). This situation also promotes higher melt fractions, as more melt accumulates within the host matrix (Fig.

15

Table 1: Source composition used in the simulations of Figs. 2 and 3.

Major	wt%	Trace	ppm	Trace	ppm
SiO_2	44.59	La	0.192	Tb	0.070
Al_2O_3	4.00	Ce	0.550	Dy	0.505
FeOt	8.39	Pr	0.107	Ho	0.115
MgO	38.43	Nd	0.581	Er	0.348
CaO	3.46	Sm	0.239	Yb	0.365
Na_2O	0.30	Eu	0.096	Lu	0.058
Cr_2O_3	0.57	Gd	0.358		

2.c). Simulations shown in Fig. 2.h and i indicate that increasing W_0 from 1 to 10 results in both higher melt fractions and larger Δv. Note that the slight variations in mineral phase proportion observed in Figs. 2.e and j are exclusively due to variations in melt fraction.

Figure 3 shows normalised trace element concentrations of liquids along the melting path (colour-code ranges from blue – onset of melting, to red – end of melting), and averaged liquid compositions (red dots), for the same reference values as in Fig. 2 (i.e. melting occurring within the spinel-stability field). Each of the rows corresponds to increasing values of k_0, W_0 and R_j, respectively. For ease of comparison, black dots in each panel indicate average liquid compositions of the previous panel (e.g. black dots in h refer to the red dots in g). For the reference diffusion-dependent exchange rate constant ($R_j = 10^{-12}$ m^2/s), increasing values of k_0 and W_0 barely affect the liquid compositions, whereas they vary significantly for different values of R_j. When R_j is small (i.e. under disequilibrium conditions, Fig. 3.g), trace elements cannot be fully extracted from the solid residue due to their sluggish kinet-

ics. Consequently, trace element concentrations in the melt are lower than those obtained with higher diffusivities under equilibrium conditions (Fig. 3.i). Differences between concentrations obtained with low and high diffusivities, however, vary with depth. Liquids quickly become more depleted at the onset of melting (i.e. the spacing of blue lines in Fig. 3.g is high), where the effect of disequilibrium is most noticeable. Here, incompatible elements behave less incompatibly (e.g. La behaves as if it had a higher partition coefficient), while compatible elements appear less compatible (Iwamori, 1993). On the contrary, liquid compositions are indistinguishable at shallow depths (red lines). Therefore, longer melting columns will tend to dampen the effect of diffusional disequilibrium on averaged liquid compositions, as the contribution of melts from shallower depths is more significant. Figures for equivalent melting experiments within the garnet-stability field can be found in the electronic annexes.

3. Inverse problem

So far we have focused on the physical model of melting that will be used to predict observations (i.e. melt compositions) as a function of melting conditions at depth. This physical model is referred to as the *forward problem* and is a fundamental component of any inverse problem. We now turn our attention to the formulation of the latter.

3.1. Bayesian formulation of the inverse problem

In contrast to deterministic inversions where single "best-fitting" models are sought, probabilistic formulations are based on the idea of recasting the inverse problem in the form of a statistical inference problem (see e.g.

17

Tarantola, 2005; Kaipio and Somersalo, 2005). The main question to answer therefore changes from *what is the value of variable m_o?* to *what do we know about m_o?*. In doing so, information on the uncertainties associated with observable data $\mathbf{d}$ (e.g. La content of a volcanic rock) and prior information on model parameters $\mathbf{m}$ (e.g. mantle potential temperature) are coded into probability density functions (PDFs). These represent our degree of confidence or knowledge about $\mathbf{d}$ and $\mathbf{m}$, prior to looking at actual data. Bayes' theorem then allows us to update our prior knowledge by making use of actual measurements and a physical theory that maps $\mathbf{m}$ into $\mathbf{d}$ (i.e. the forward problem). This updated state of knowledge, which represents our confidence in $\mathbf{m}$ after we have acquired data, is the formal solution to the inverse problem and is described by the so-called *posterior* PDF $\sigma(\mathbf{m})$. For parameter estimation problems, the posterior PDF can be written as

$$\sigma(\mathbf{m}) \propto \mathcal{L}(\mathbf{m})\rho(\mathbf{m}) \tag{15}$$

where $\rho(\mathbf{m})$ is the prior PDF of the model parameters and $\mathcal{L}(\mathbf{m})$ is the *likelihood* function, a measure of how well the model explains the observations (Tarantola, 2005). Since $\mathcal{L}(\mathbf{m})$ contains the forward problem, its actual form depends on assumptions made about the statistics of the noise affecting both data and model predictions; we discuss these in the next section (see also Fig. 1 in the electronic annex).

In the most general case of high-dimensional and non-linear problems with complex priors, the only practical solution for Eq. 15 is based on the construction of a Markov chain that has $\sigma(\mathbf{m})$ as its equilibrium or stationary distribution (cf. Kaipio and Somersalo, 2005; Brooks et al., 2011). Markov chain Monte Carlo (MCMC) algorithms are designed to produce un-

18

biased approximations of the true posterior by repeatedly drawing models m_1, m_2...m_n and evaluating their posterior probabilities (i.e. solving the forward problem, further details in Appendix B). An acceptance criterion is used to decide whether proposed models are rejected or accepted as part of the chain. The reader is referred to the monographs by Kaipio and Somersalo (2005), Liu (2008) and Brooks et al. (2011) for further details on the construction of MCMC algorithms. Here we use the Adaptive Metropolis algorithm of Haario et al. (2001).

3.2. Uncertainties and likelihood

An important aspect of probabilistic formulations is the explicit treatment of uncertainties in both observations and physical theories. In most situations, uncertainties affecting the observations are straightforward to estimate and/or model. A Gaussian model is commonly justified and used. Theoretical uncertainties, however, are typically much more difficult to quantify, especially in cases where the forward model is complex.

3.2.1. Uncertainties in compositional data

A standard tenet of analytical geochemistry is that results from measurements can be reported as a summary statistic (e.g. the mean) together with an associated measure of dispersion. The most common distribution assumed for the measurements is a Gaussian. Therefore, we can describe the uncertainties of a given data vector $\mathbf{d}$ of dimension n as a probability density ρ_D given by

$$\rho_D = [(2\pi)^n \det(C_D)]^{-1/2} \exp\left(-\frac{1}{2}(\mathbf{d} - \mathbf{d}^{\mathrm{obs}})^{\mathsf{T}} C_D^{-1}(\mathbf{d} - \mathbf{d}^{\mathrm{obs}})\right) \qquad (16)$$

19

where $\mathbf{d}^{\mathrm{obs}}$ is the vector of measured values, n is the dimension of $\mathbf{d}^{\mathrm{obs}}$ and C_D is the covariance matrix. In this expression we implicitly assume that the natural variability of the specific suite of volcanic rocks under study and any sample preparation biases/errors are accounted for and can both be conveniently represented with Gaussian statistics (Miesch, 1967). In this favourable case, the additivity property of the variance allows the combination of covariances of all sources of error into a single term $C_D = C_{sampling} + C_{preparation} + C_{analytical}$. The question of whether Gaussian noise statistics for all sources of error is appropriate for geochemical data is contentious and beyond the scope of this paper. Here we simply assume that one can have access to $C_{preparation}$ and $C_{analytical}$ for all data types (e.g. from analytical measurements) and that $C_{sampling}$ can be at least estimated.

3.2.2. Modelling uncertainties

Errors associated with deterministic numerical models are not random, but rather they are controlled by systematic biases (e.g. underestimation due to simplifying assumptions) and human errors (e.g. 'bugs' in the code). A common example of a systematic error is that related to the coarseness of the numerical mesh used in the discretization of the governing equations (i.e. coarse meshes are less accurate than fine meshes). Well-known procedures are available in the literature to estimate these type of errors (Smith, 2013; Gürlebeck et al., 2020), which for no other reason than convenience, we will refer to as *numerical* errors. In contrast, uncertainties associated with the actual theoretical or physical conceptualization used to make predictions (the forward model) are less objective and far more complicated to assess. This is at least partially due to the inherent difficulty in assigning errors

20

to an arbitrary conceptualization of a natural process that we do not fully understand. We refer to this type of uncertainty as *model* uncertainty (see Ayyub and Klir, 2006; Smith, 2013; Gürlebeck et al., 2020 for more general treatments on uncertainties affecting modelling).

While neither numerical nor model uncertainties are routinely accounted for in studies of mantle melting, it is instructive to at least attempt to quantify or estimate their effects on our interpretations of data. We note that ignoring numerical and model uncertainties implies that our physical model and its numerical solution are considered a perfect description of the melting process of interest, which results in unrealistic confidence in the model's predictions. We studied numerical errors affecting our forward problem using extensive numerical experiments (e.g. testing different discretizations, different numerical meshes, etc). We then combined these results with the uncertainties associated with the thermodynamic solver used to make predictions of mineral assemblages. These uncertainties were taken from the uncertainty analysis in Afonso et al. (2013a). The combination of these two sources of uncertainty gives an estimate of total (numerical+modelling) uncertainty of 3–10% and 6–16% for the computed major and trace element compositions, respectively. The variability in these estimates is associated with different elements. Uncertainties arising from errors in the selection of partition coefficients are addressed in Section 4.4.

Assuming Gaussian error statistics for both observed and predicted data, $L(\mathbf{m})$ can be expressed as (Tarantola, 2005)

$$L(\mathbf{m}) \propto \exp\left(-e(\mathbf{m})\right) \tag{17}$$

21

where $e(\mathbf{m})$ is the sum-of-squares function, which acts as a misfit function between observed and predicted data. It is computed as

$$e(\mathbf{m}) = \frac{1}{2}(\mathbf{d}^{\mathrm{pre}} - \mathbf{d}^{\mathrm{obs}})^{\mathsf{T}} \mathrm{C}_{\mathrm{D}}^{-1}(\mathbf{d}^{\mathrm{pre}} - \mathbf{d}^{\mathrm{obs}}) \tag{18}$$

where $\mathbf{d}^{\mathrm{pre}}$ represents the prediction from the forward problem for model $\mathbf{m}$ and C_D is the covariance in Eq. 16, with an extra term accounting for modelling uncertainties (Tarantola, 2005).

3.3. Parameterization of the forward problem

As in any other inversion problem, our chosen parameterization is a compromise between the following features: flexibility to incorporate prior information, modify the forward model and extract by-product information, parsimony of the parameter space, identifiability of the main parameters, computational simplicity and fit to purpose (i.e. suitability for the problem of interest). With these principles in mind, and considering the results summarised in Figs. 2 and 3, we choose to define the following model parameters:

- Mantle potential temperature, T_p. This parameter exerts first-order control on the initial depth of melting and it determines the magnitude of the thermal anomaly triggering partial melting. We clarify that this parameter is the temperature that the upwelling solid would attain if it reached the surface without experiencing melting.

- Depth at which melting stops, Z_{top}. This depth is assumed to be a reasonable proxy for the base of the lithosphere (i.e. the thermal boundary layer). In the context of upwelling mantle, Z_{top} is the depth at which the original upwelling, responsible for the generation of the melt, is

22

horizontally deflected after impinging on the base of the cold thermal boundary layer. We therefore assume that the process of isentropic decompression melting stops at Z_{top}.

- The major and trace element composition of a peridotitic mantle source. The mantle trace element content, by which we mean REEs in particular, is not always correlated with that of major elements (e.g. an "enriched" signature in traces can co-exist with a "depleted" signature in majors). We therefore treat these two different groups of elements as independent. In contrast, correlations exist within each group. This is particularly true in the case of major elements in peridotites (Afonso et al., 2013a). Taking advantage of these correlations, Afonso et al. (2013a,b) proposed a general approach to reduce the number of compositional parameters in thermodynamically-constrained probabilistic inversions of geophysical data. Here we adopt a similar strategy and choose only two independent elements to characterise the first-order major element composition of the source: Al_2O_3 and Na_2O (see Appendix B). Al_2O_3 is a proxy for melt depletion or refertilization and can be used to reconstruct the CFMAS composition of the source (e.g. Afonso et al., 2013a, 2016). Na_2O is not necessarily well correlated with Al_2O_3, but it has a significant impact on the position of the solidus (Jennings and Holland, 2015), and therefore, on the computed compositions. Note that despite not shown in this study, the code provided in Oliveira et al. (2021) allows to model all major elements according to the probabilistic approach in Afonso et al. (2013a).

23

4. Inversion results using synthetic examples

To illustrate the inversion approach and its sensitivity to model parameters of interest, we generated synthetic data sets of melt compositions using the forward model of Section 2. The parameters defining the true model used in the examples below are listed in Table 2. For simplicity, we consider a constant R_j of 10^{-12} s^{-1} for all mineral phases and trace elements, equivalent to average diffusion coefficients of $\sim 10^{-16}$ m^2/s and spherical grain sizes of 3 mm. The permeability constant is set to 10^{-8}, and the exponential factor n is equal to 3. We set $Z_{top} = 70$ km and $T_p = 1400$ °C. The melting column that results is within the garnet field, it spans a depth range of 70–80 km and reaches a total melt fraction of $\sim 6\%$ (Fig. 4). The synthetic data is composed of the contents of major elements SiO$_2$, Al$_2$O$_3$, FeO, MgO, CaO, Na$_2$O, Cr$_2$O$_3$ as well as those of trace elements La, Ce, Pr, Nd, Sm, Eu, Gd, Tb, Dy, Ho, Er, Yb and Lu. We then invert these data to assess melting conditions and source composition in the presence of realistic uncertainties. Other model predictions, such as total melt production or the composition of the residual phases, can be readily used instead if desired. Priors for all parameters used in this section are listed in Table 2.

4.1. Inversion of trace elements only

Figure 5 shows the posterior PDFs resulting from inverting the trace element composition of the synthetic lava for parameters Z_{top} and T_p only (i.e. the shape of the melting regime). We have assumed perfect knowledge of all other model parameters and/or variables that may affect the final composition of the erupted lava (e.g. major and trace element source composition,

24

mineral modes along the melting path, partition coefficients, etc). For simplicity, we assume constant partition coefficients of trace elements between all mineral phases and melt as specified in Oliveira et al. (2020); we relax this assumption in later examples.

The posterior PDFs in this example are well-behaved (i.e. single minimum, small dispersion, approximately normally distributed) and they include the true solution within their high probability regions (red distributions in Fig. 5). This demonstrates that trace element composition alone is sufficiently sensitive to the sought model parameters when all other parameters are set to their true values. The question that arises is whether the same can be said for the more realistic case when we do not perfectly know other parameters that influence the evolution of the melting regime. The answer to this question is illustrated in Fig. 5, where we also show the results of repeating the inversion for Z_{top} and T_p, but assuming an "incorrect" source composition (green distributions). Since the true source composition is representative of primitive mantle (see Table 1), we created the "incorrect" source by simply assuming a more depleted composition. Specifically, we mixed equal amounts of PM and DMM components to create a depleted trace element composition and reduced the Al_2O_3 and Na_2O contents by a modest 0.7% and 0.1%, respectively. While the resulting posterior PDFs remain well-behaved and localised (which gives a false sense of certainty), the actual true values are outside the region of high probability (in fact, the true results are in a region of zero probability according to the posterior PDFs). For comparison, we also include in Fig. 5 the solution from a deterministic inversion using the non-linear least-squares algorithm known as the Quasi-Newton method (c.f.

Tarantola, 2005; Afonso et al., 2019). The deterministic solution converges quickly (only 10 iterations were needed to achieve $< 0.5\%$ relative variation in model parameters) and produces a stable and single-valued solution, albeit the incorrect one.

The above problem is better illustrated when we explicitly account for uncertainties in the source composition. For instance, Fig. 6a shows the posterior PDFs of an identical inversion to those described above, but allowing for some variability in the major element composition of the source in the form of prior PDFs. One of the most important results of this test is the clear trade-off between Z_{top} and T_p. While the true Z_{top}-T_p values are contained in the region of high probability, the solution is highly non-unique (i.e. any Z_{top}-T_p combination along the PDF in Fig. 6a is an acceptable solution). In other words, the trace element composition of a pooled melt produced within a deep melting regime (i.e. high T_p and large Z_{top}) is indistinguishable from a melt with similar F produced within a shallower melting regime (i.e. lower T_p and smaller Z_{top}). This is true provided that i) we allow for some uncertainty in the major element composition of the source and ii) both melting columns reside entirely within either the garnet (as in the present case) or the spinel stability field. Perhaps not surprisingly, Figure 6a also shows that the sensitivity to the major element composition of the source is poor.

The trade-off between Z_{top} and T_p can be explained as follows. Eq. 7 states that the trace element concentration of the aggregated melt along the melting regime (c_{iso}^b) is controlled by i) the local mineral assemblage experiencing partial melting (via c_{inst}^b; Eqs. 3 and 8) and ii) the rate of melting Γ. This effectively means that melting regimes with similar residual

26

mineral phases and melting rates, irrespective of depth and temperature, can produce similar trace element contents of their aggregated melts. Moreover, since the final melt compositions are a weighted averages (Eq. 14), we lose some information about the pressure range over which the melting occurred.

An obvious question that arises from the above observations is whether introducing pressure, temperature and/or compositional dependence (P-T-C) on the partition coefficients can minimise the problem of non-uniqueness in Z_{top} - T_p space. To test this, we adopted the model of Wood and Blundy (1997) for clinopyroxene and that of Van Westrenen et al. (2001) for garnet. The posterior PDFs of an inversion using these P-T-C-dependent partition coefficients are shown in Fig. 6b. We can see that the large trade-off between Z_{top} and T_p in Fig. 6a is indeed reduced due to the additional sensitivity to pressure, temperature and melt composition introduced via the partition coefficients of clinopyroxene and garnet (cf. Wood and Blundy, 2014). Unfortunately, the sensitivity to the major element composition of the source remains very poor.

4.2. Inversion of major elements only

In this example, we explore the sensitivity to Z_{top}, T_p and major element source composition when the data to be inverted is the major element composition of the pooled (primitive) melt. Given the greater sensitivity of major elements to the pressure range at which the melt is produced (e.g. Langmuir et al., 1992; Herzberg and O'Hara, 2002; Herzberg, 2004; Jennings and Holland, 2015), we expect a better performance at recovering Z_{top} and T_p, even when using constant partition coefficients. The priors for Z_{top} and T_p are the same as in the previous example; those for source composition

27

are $0.2 < Al_2O_3 < 4.6$ wt% and $0.01 < Na_2O < 0.7$ wt%. Figure 7 shows the posterior PDFs for all four model parameters. As expected, the space of acceptable model parameters is greatly reduced compared to the results in Fig. 6. More importantly, not only the trade-off between Z_{top} and T_p is now considerably smaller but it also reverts its trend (i.e. a positive correlation becomes a negative one). This quasi-orthogonal behaviour of the two different compositional data sets is a highly desirable feature in the context of joint inversions, as trade-offs in the parameter space cancel each other out, leaving a much more localised region of high probability where the two independent posterior PDFs intersect.

The posterior PDFs for composition are now better behaved and contain the true solution in their regions of high probability, even when the uncertainties assigned to the synthetic data are relatively large. These results clearly demonstrate and validate the value of major elements for estimating melting conditions. Unfortunately, primary major element compositions can change significantly during ascent and storage of a magma (e.g. via fractional crystallisation), complicating the use of major elements in real applications. We discuss the issue of how to obtain representative parental/primitive magma compositions from natural samples in the electronic annex.

4.3. Joint inversion of major and trace elements

The observations summarised above suggest that there can be significant gain in sensitivity to melting conditions (including source composition) by jointly inverting trace and major element contents of primitive lavas. In this last example we show the results of such an inversion when using P-T-C-dependent partition coefficients. Importantly, the general observations and

conclusions are not changed by assuming constant partition coefficients.

4.3.1. Joint inversion for Z_{top}, T_p and major element composition of the source

Figure 8 shows the posterior PDFs for Z_{top}, T_p, Al_2O_3 and Na_2O. It is clear that even when allowing for generous uncertainties in both observations and predictions, all parameters are well constrained and the probability functions are well behaved. The gain of information, measured as the ratio between the posterior and the prior PDFs, is higher in this case than in any of the previous examples.

4.3.2. Joint inversion for Z_{top}, T_p, major and trace element composition of the source

Here we expand the parameter space to include thirteen REEs, making the final parameter space to be seventeen-th dimensional. The chosen priors for the REEs are wide enough to include all estimates of mantle sources, from extremely depleted to primitive mantle (Table 2). For clarity and space reasons, we only plot the marginal PDFs for each parameter in Fig. 9; full joint distributions and correlations between parameters are plotted in the electronic annex. It can be seen that the posterior PDF sampled during the MCMC simulation contains the true solution within its region of high probability. In particular, the mean values of the marginals of Z_{top}, T_p and Na_2O are almost identical to the true values. For Al_2O_3 and trace elements, however, we observe a slight, yet systematic, shift towards higher mean values relative to the true ones. Given the complex, high-dimensional and non-linear character of the forward problem, it is difficult at this time to isolate the

29

main causes for this deviation. However, we emphasise that for all practical purposes, this deviation is immaterial when we consider the actual gain of information for all parameters (i.e. the conversion from prior to posterior). Moreover, all true values are within 1 STD from the mean of the marginal distributions.

4.4. Errors in partition coefficients

An important source of uncertainty in our computed compositions arise from uncertainties in the actual values of the melt-solid partition coefficients for each mineral phase. Reported values vary greatly in the literature (https://earthref.org/GERM/), especially when comparing estimates derived from laboratory experiments with those from observations in natural assemblages. However, if we restrict the focus to experimentally-derived values, the disagreement between commonly accepted compilations is significantly reduced; we take these discrepancies as representative of the uncertainty in partition coefficients whether they are assumed constant or derived from a P-T-C-dependent model. Note, that at least part of the variations in experimentally-derived partition coefficients as listed in GERM results from differences in P-T-C experimental conditions rather than from intrinsic measurement errors. The uncertainties presented below should therefore represent upper bounds.

In order to quantify the propagation of errors into our computed compositions, we perform a global uncertainty analysis based on Monte Carlo simulations. The melting column we choose for the numerical simulations is identical to the ones used in previous examples. We randomly vary the partition coefficients of all elements in clinopyroxene and garnet within a generous,

yet realistic, uncertainty of 25% (as 1 STD; thus a total allowed variation of $\sim 100\%$). As before, we do not vary the partition coefficients in olivine, orthopyroxene and spinel, as their effect is only second-order compared to that of clinopyroxene and garnet.

The results of these simulations are summarised in Table 3. In general, the propagated error to computed trace element compositions is of the order of 10–24% (as 1 STD), with the larger values associated with the heavy REEs. These uncertainties are comparable to those arising from the natural variability in the data when analysing multiple samples in one region (e.g. Klöcking et al., 2018) and therefore they should be considered when inverting real data.

5. Application to samples from the Rio Grande Rift, USA

5.1. Data and background

In this section we apply our method to a well-studied, real data set from the Rio Grande Rift in western North America. The Rio Grande Rift forms a >600 km long, N-S trending intracontinental rift valley associated with significant lithospheric extension and voluminous Miocene mafic volcanic rocks (Tweto, 1979). Rifting and volcanism were initiated at $\sim$30 Ma when subduction of the Farallon slab ceased (Christiansen and Lipman, 1972). Numerous previous studies have investigated lithospheric thickness, mantle potential temperature and magmatic source compositions of the Rio Grande Rift (e.g. Thompson et al., 2005; Afonso et al., 2016; Hopper and Fischer, 2018), which makes it an ideal region to test our modelling framework. In particular, there is evidence of a mantle upwelling with elevated asthenospheric poten-

tial temperatures beneath the region, that triggered magmatic activity and large-scale regional uplift (e.g. Thompson et al., 2005; Klöcking et al., 2018).

We use a subset of 49 sample compositions from the volcanic data compiled in Klöcking et al. (2018). All samples contain MgO $\geq$9 wt% to minimise the effect of crystal fractionation on lava compositions. In addition, the data set has been screened by La/Ba and La/Nd ratios to remove samples with a subduction signature attributed to a lithospheric mantle source (Fitton et al., 1991). Since there is evidence of clinopyroxene fractionation in samples with <10.7 wt% MgO (Thompson et al., 2005), we correct major and trace element compositions through reverse crystallisation of clinopyroxene in Petrolog3 (Danyushevsky and Plechov, 2011). Beyond the threshold of 10.7 wt% MgO, the major element compositions of all samples are further corrected for olivine fractionation by incremental addition until the Ni content of olivine in equilibrium with the corrected melt reaches 3500 ppm (Korenaga and Kelemen, 2000). Observed REE concentrations are subsequently corrected for the amount of olivine addition by mass balance, assuming that olivine contains no REEs. Further details of the clinopyroxene and olivine fractionation corrections used here are reported in the electronic annex. We also note that all samples fall well within the peridotite-derived fields according to multiple proxies (e.g. FC3MS, FCKANTMS; Yang et al., 2019) and therefore contributions from a pyroxenite mantle source should be insignificant. The mean of these corrected sample compositions is then inverted for source composition, depth of melting and potential temperature. The priors used in the inversion are listed in Table 2.

For the forward problem we consider partition coefficients from Wood

and Blundy (1997) and Van Westrenen et al. (2001) for cpx and grt, respectively. Partition coefficients for the rest of mineral phases, as well as the P-T dependant diffusion coefficients, are taken from Oliveira et al. (2020). Unlike in previous examples, mineral grain size varies between phases (3, 1, 2.5, 1, 1 and 1 mm for ol, cpx, opx, grt, sp and pl, respectively). The remainder of model parameters (e.g. permeability) are the same as in the previous synthetic examples.

5.2. Data fits

Figure 10 shows the model fits to the data. This fit is excellent for all REEs, with the mean of the input data falling within one standard deviation of the marginal posterior PDFs (Fig. 10.a). The same is true for major elements except Al_2O_3 and MgO, whose posterior PDFs overlap with the observed distribution at the level of two standard deviations (Fig. 10.b). In the case of Al_2O_3, predicted values are slightly higher than the observed concentrations, whereas the opposite is observed for MgO. Since the Al_2O_3 and MgO contents of primitive melts decrease and increase, respectively, with increasing potential temperature and amount of melting (e.g. Herzberg, 2004; Jennings and Holland, 2015), the inversion could in principle push towards higher values of T_p to deliver better fits to these two oxides. However, the resulting depletion trend in the REEs would not fit the data as well, even when the REE composition of the source is allowed to vary. The requirement of acceptable joint fits to both major and trace element compositions thus precludes solutions with higher degrees of melting.

Other factors may be contributing to the modest misfit of Al_2O_3 and MgO. Foremost among these are inaccuracies in the fractionation correction.

33

It is possible that sample compositions were over-corrected both for clinopyroxene and olivine fractionation in the simplified approach taken here. The threshold for clinopyroxene addition of 10.7 wt% MgO is merely an empirical value and the Ni content of parental olivine could be as low as 2000 ppm (Korenaga and Kelemen, 2000). Assimilation of country rock could also alter observed compositions. While there is no isotopic evidence of crustal contamination, Thompson et al. (2005) report partially resorbed xenocrysts in some of the lavas studied here. In a small portion of samples, Thompson et al. (2005) also observe evidence of amphibole, a hydrous phase, in the source assemblage. The presence of volatiles in the source could produce a deep tail of low-degree melt with lower Al_2O_3 and higher MgO contents. However, this effect will be largely diluted in the accumulated melt. While volatile-rich melting would help to reconcile the misfit, its effect is likely small and would affect REEs more substantially than the major elements. Lastly, if melts partially reacted with peridotites in the lithospheric mantle, olivine could have been consumed to create orthopyroxene (e.g. Mallik and Dasgupta, 2012). This would have decreased the Al_2O_3 content of the melt and increased its MgO content (Mallik and Dasgupta, 2012; Liu et al., 2016) without affecting the REE contents to any significant extent. We emphasise that the effect of these potential factors on our model results is small and that the overall fit to data is good. Taken together with the geophysical evidence discussed below, further exploration of these more complex processes seems unwarranted.

34

5.3. Results

The posterior distributions of the main model parameters are summarised in Fig. 11 as a covariance plot of joint distributions. For space reasons, we only show three representative REEs (La, Sm and Lu). The complete set of results is included in the electronic annex. The posteriors for T_p and Z_{top} show a clear single peak of high probability, centered at $\sim$ 1338 °C and 60 km, respectively. The value for Z_{top} is in excellent agreement with recent estimates of lithospheric thickness from Sp converted seismic waves (Hopper and Fischer, 2018), multi-observable thermochemical tomography (Afonso et al., 2016) and a deterministic inversion strategy applied to volcanic REEs (Klöcking et al., 2018). The value for T_p obtained here is indicative of a moderately hot mantle upwelling and well within the range of potential temperatures ($\sim$ 1320–1400 °C) derived from the models presented in Afonso et al. (2016), Thompson et al. (2005) and Klöcking et al. (2018).

The REE source composition retrieved by the inversion indicates a relatively enriched source in light and middle REEs, that is close to 'primitive mantle' estimates (Fig. 10 and electronic annex). Heavy REEs, however, exhibit a more depleted character. In terms of major elements, the source shows moderate levels of depletion. Taken together, these observations suggest that the alkali basalts used in this study are derived from a slightly depleted source that experienced a small degree of melt or fluid metasomatism, resulting in relative enrichment of the light and middle REEs compared to the heavy REEs.

Considering all of the above, two scenarios seem possible. In one, most or all of the melt is generated within a shallow sublithospheric upwelling with

the compositional characteristics summarised in Figs. 11 and 10. This mantle source could be lithologically heterogeneous, although any contribution from a recycled component must be minimal. In the other scenario, the volcanic rocks studied here contain contributions from melts generated within i) a more fertile shallow sublithospheric upwelling and ii) the lower portions of the more depleted and metasomatised lithospheric mantle; here we use the terms fertile and depleted to refer to the major element composition. Discerning between these two scenarios is not only beyond the scope of this paper, but also not possible based on the inversion results alone. However, we note that Thompson et al. (2005) presented an interpretation similar to our second scenario to explain some peculiar petrological and isotopic characteristics in samples from the Potrillo Volcanic Field. In this context, we note that although the samples used for inversion were screened to remove 'subduction signatures', metasomatic enrichment by other melts or fluids may be difficult to identify. It is encouraging, therefore, that the modelling framework introduced in this paper can resolve such subtle processes.

6. Discussion

In this work we approximate melt production with a one dimensional isentropic fractional fusion model, where liquids are isolated from the solid as soon as they are produced and mixed with previously extracted melts. However, various lines of evidence show that chemical equilibration may occur between residual solid and trapped melts (Kent, 2008, and references therein). When modelling isentropic fractional melting, the degree of melting, F, is dictated exclusively by the evolution of the solid's major element

36

composition and entropy (or temperature). If trapped melts are present, their compositions and entropy should also be considered when computing F. Given the inter-dependency between chemical composition and degree of melting (e.g. Asimow, 2001), any model ranging between the end-members of batch and fractional melting will result in different predictions of melting conditions and source compositions. Although not shown here, the melting model presented in this paper can be readily modified to account for trapped melts (see electronic annex and Oliveira et al., 2020 for further details). Similarly, the inclusion of isotopes as part of the data vector and melting model (e.g. Brown et al., 2020) is possible and will be explored in future implementations.

In addition, our estimate of the degree of melting depends on the thermodynamic model chosen for the liquid and solid phases. For instance, despite their well-known effect in lowering the solidus, volatiles were not included in the current anhydrous thermodynamic model (Jennings and Holland, 2015). More recent thermodynamic models have included volatiles but are yet to be fully calibrated for large pressure, temperature and compositional ranges (Holland et al., 2018). Likewise, thermodynamic solvers like pMELTS (Ghiorso et al., 2002), which includes volatiles and its own thermodynamic database, offer attractive alternatives. Although a detailed comparison between thermodynamic softwares and/or databases is beyond the scope of this paper (cf. Stolper et al., 2020), the electronic annex includes a comprehensive summary of the mineral distribution, solid and melt chemistry as a function of pressure, temperature and chemical composition used in this paper and obtained with Perple_X using the thermodynamic model from

Jennings and Holland (2015). Future applications of our method should test the use of these thermodynamic models.

Perhaps the most important limitation of the current implementation of our method is that we only model a homogeneous source composition (peridotite). This requires natural samples to be carefully screened to remove those with significant contributions from lithologies other than peridotite (e.g. pyroxenite). Otherwise, temperature, pressure and source composition estimated by the inversion will not be representative of the actual melting conditions. Nonetheless, regardless of whether there is a pyroxenitic component present in the volcanic field under study, as long as we can identify a number of samples that have been produced from the peridotitic component (e.g. using FC3MS, FCKANTMS or multi-phase projections), the inversion will provide reliable results in terms of the first-order thermochemical state of the upper mantle. In order to model an heterogeneous source, the aggregate solid needs to be modelled as different subsystems (Brown et al., 2020; Oliveira et al., 2020) and additional assumptions regarding the way these subsystems interact thermally, mechanically and chemically are required. We are currently working on this topic and the results will be presented in a forthcoming publication.

In addition to the improvements discussed above, the present model is well-suited for joint geophysical-geochemical characterization of the upper mantle beneath regions where recent basaltic volcanism took place. The combination of an internally-consistent thermodynamic model with our forward melting model allows retrieving complete sets of physical and chemical properties that can be used to jointly predict geophysical and geochemical ob-

servables. The implementation of the forward model presented in this work in geophysical probabilistic approaches (e.g. Afonso et al., 2013a,b; Khan et al., 2013) would thus allow to fully exploit the complementary sensitivities of geophysical and geochemical data sets to the thermochemical structure of the mantle (e.g. Afonso et al., 2016).

7. Conclusions

We present the first probabilistic inverse approach for the joint inversion of major and trace element data of mafic volcanic rocks to assess melting conditions, degree of melting and source composition in the upper mantle. To do so, we combined i) a two-phase, disequilibrium model of melt generation and transport, ii) a thermodynamic solver that describes the local partitioning of major elements into mineral/liquid phases, (iii) a disequilibrium model of trace element partitioning, and iv) a Markov chain Monte Carlo inversion scheme.

Using numerical experiments, we have shown that the thermodynamically- and internally-consistent joint inversion of REEs and major elements is widely applicable and has a unique sensitivity to mantle temperature, pressure range of melting and source composition, even when all main sources of uncertainties in both data and model predictions are considered. It can thus be used to study the evolution of the lithosphere-asthenosphere system, and that of the upper mantle in general, through time. We confirm that the use of P-T-C-dependent partition coefficients for REEs is absolutely necessary when inverting these elements alone, as their content in the aggregated melts is largely insensitive to the pressure range of melting when the source compo-

39

sition is uncertain and melting occurs entirely within the spinel or garnet stability fields. This lack of sensitivity disappears when major elements are included in the inversion, even if constant partition coefficients are used.

Tested on a well-known natural dataset from the Rio Grande Rift, this new approach yields predictions of mantle potential temperature, lithospheric thickness, and mantle composition that are in excellent agreement with numerous independent results from geochemical and geophysical studies. Specifically, the inversion predicts moderately high potential temperatures (~ 1340 ^oC) and a very thin lithosphere (~ 60 km). The inversion also identified a moderately depleted source in terms of major elements and a differential enrichment in the light REEs relative to the heavy REEs, which suggests i) a small degree of melt or fluid metasomatism and ii) a possible contribution from melting of the lower portions of the lithosphere.

It is worth emphasising that the selection of representative samples is a critical step in the inversion workflow. The major-element composition of a melt can change dramatically from source to surface. Therefore, samples need to be screened and/or their compositions corrected to minimise the effects of fractionation/assimilation and/or major contributions from lithologies other than peridotite. Nevertheless, the results in this paper indicate that the the joint inversion is capable of retrieving reliable estimates even when only simple screening/corrections are applied to the data.

An important spin-off of the new probabilistic framework is that it opens up the possibility of truly joint geochemical-geophysical inversions for the thermochemical structure of the upper mantle beneath regions with recent basaltic volcanism (e.g. rifted areas, MORs, OIBs, intraplate volcanic re-

gions). The inclusion of our melting model into geophysical probabilistic inversion platforms (e.g. Afonso et al., 2016) will provide a unique and formal means to assessing the nature of the discrepancies and compatibilities between geophysical *vs.* geochemical model predictions. This in turn will contribute towards generating more comprehensive and explicative models of the Earth's interior.

8. Research Data

The code to perform all calculations in this paper is published in Oliveira et al. (2021).

9. Acknowledgments

Figure 1: Schematic illustration showing the model setup. The base of the column corresponds to the onset of melting, where the upwelling solid crosses its solidus. Instantaneous melts are generated along the whole melting column (dashed blue lines), which are allowed to segregate vertically in chemical isolation (red lines). The solid is comprised of an aggregate of mineral phases, which melts isentropically until it reaches the top of the melting column (assumed to be the base of the lithosphere). More information on the melting model can be found in Appendix A.
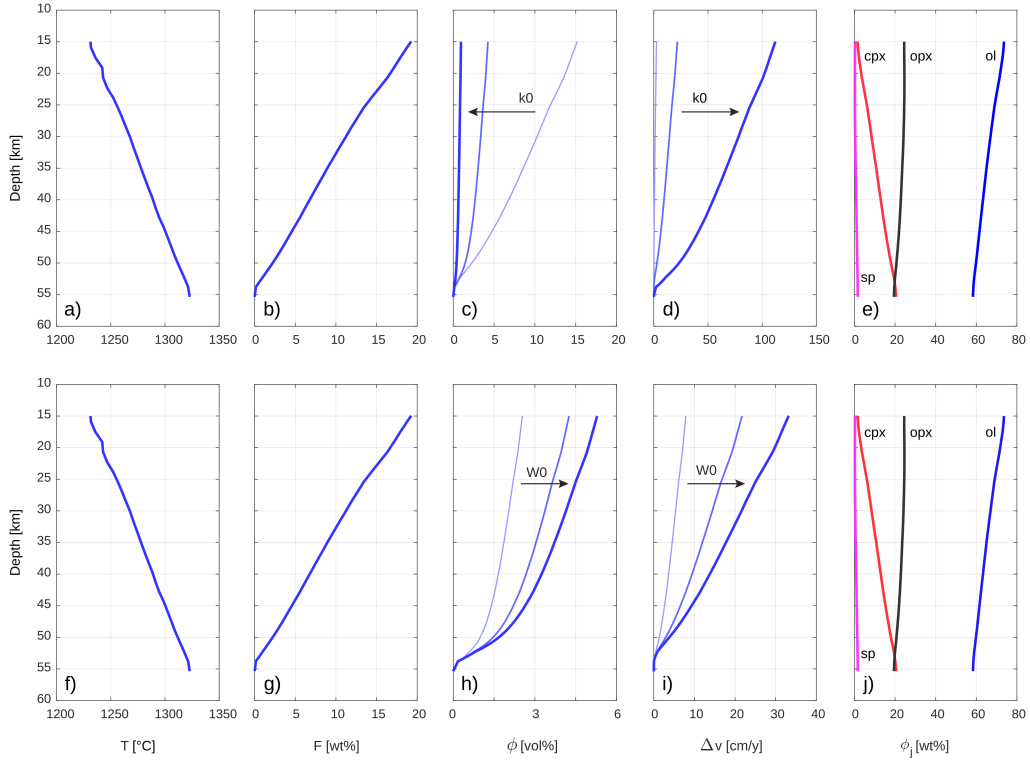
Figure 2: Results of 1D decompression upwelling simulations for different values of permeability constant, k_0 (a-e), and upwelling velocities, W_0 (f-j). Darker blue lines represent higher values of k_0 and W_0, which range from $k_0 = 10^{-10}, 10^{-8}, 10^{-6} \mathrm{m}^2$ and $W_0 = 1, 5, 10$ cm/y. Simulations assume $T_p = 1300°C$, $\mu_l = 1$ Pa s, no chemical isolation of the liquid phase, and $W_0 = 5$ cm/s and $k_0 = 10^{-8}$ for the upper and lower panels, respectively. Source compositions are given in Table 1, and partition coefficients are from Oliveira et al. (2020).

43
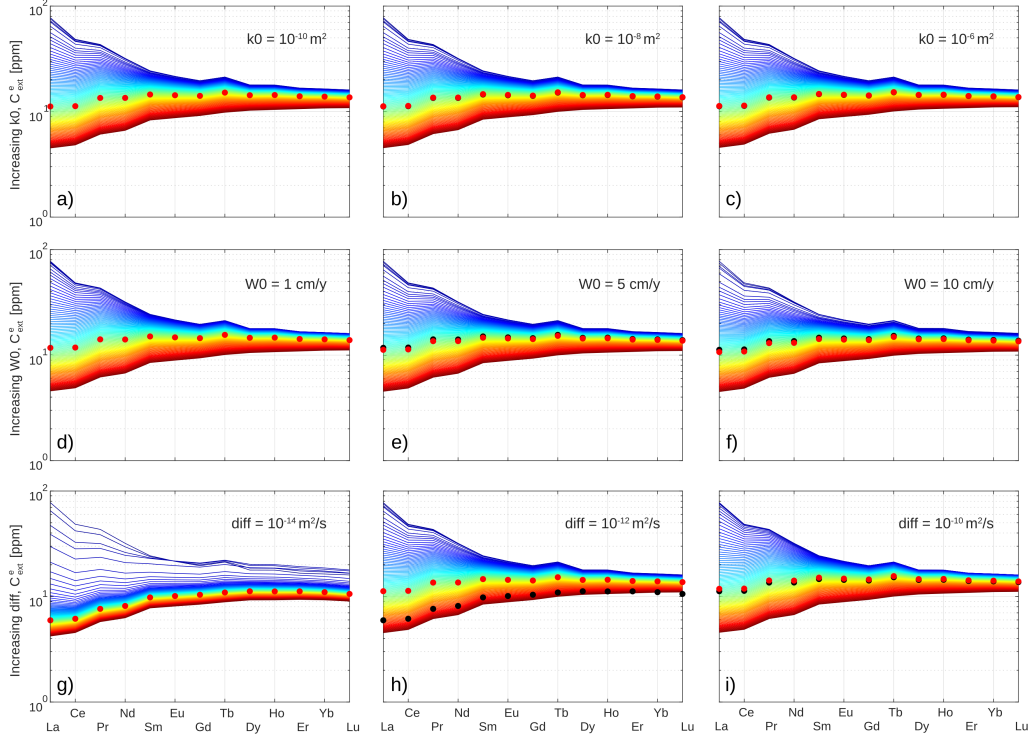
Figure 3: Normalised REE compositions in the extracted liquid along 1D decompression upwelling paths for increasing values of permeability constant (a-c; $k_0 = 10^{-10}, 10^{-8}, 10^{-6} \text{m}^2$), upwelling velocities (d-f; $W_0 = 1, 5, 10$ cm/y), and diffusivities (g-i; $R_j = 10^{-14}, 10^{-12}, 10^{-10}$ s^{-1}). Simulations assume $T_p = 1300°$C, $k_0 = 10^{-8}\text{m}^2$, $W_0 = 5$ cm/s, and $R_j = 10^{-12}\text{s}^{-1}$ as reference values. Initial compositions are given in Table 1 and partition coefficients are from Oliveira et al. (2020). Coloured lines refer to instantaneous melt compositions at variable depth, ranging from blue – onset of melting, to red – end of melting. Red dots are averaged liquid compositions computed with Eq. 14. Black dots in each panel indicate average liquid compositions from the adjacent panel to the left.
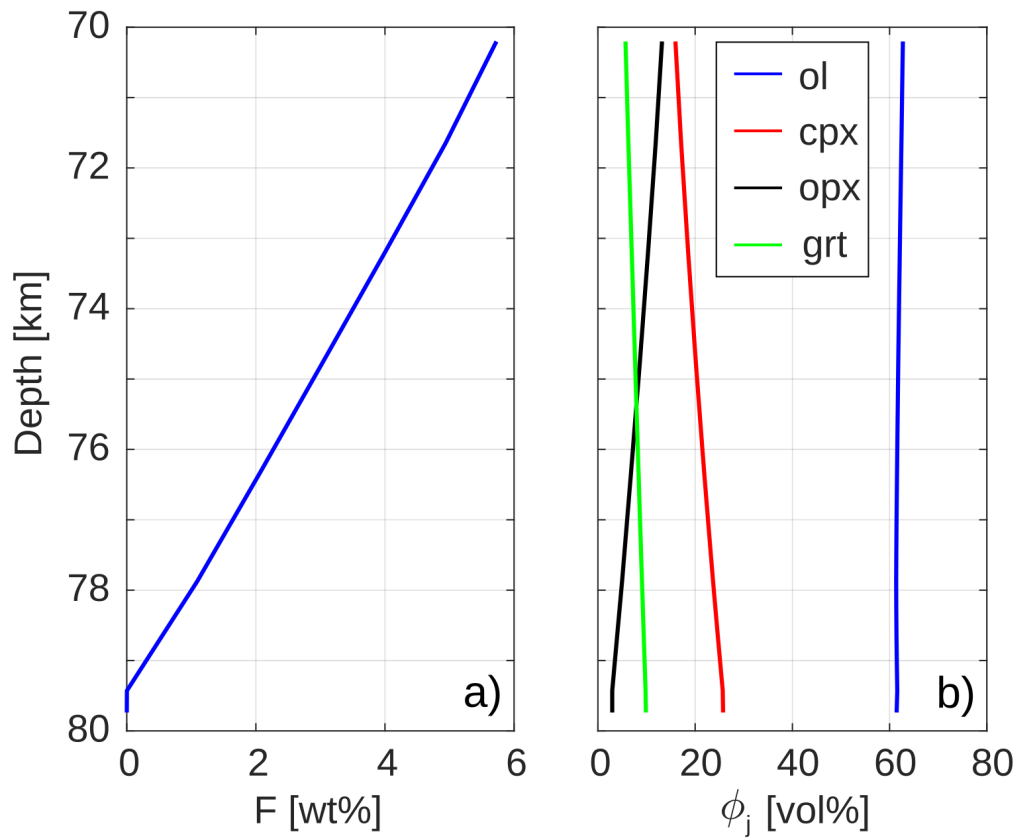
Figure 4: a) Degree of melting F and b) mineral phases as functions of depth predicted by the reference (true) model used to generate the synthetic data of Section 4.
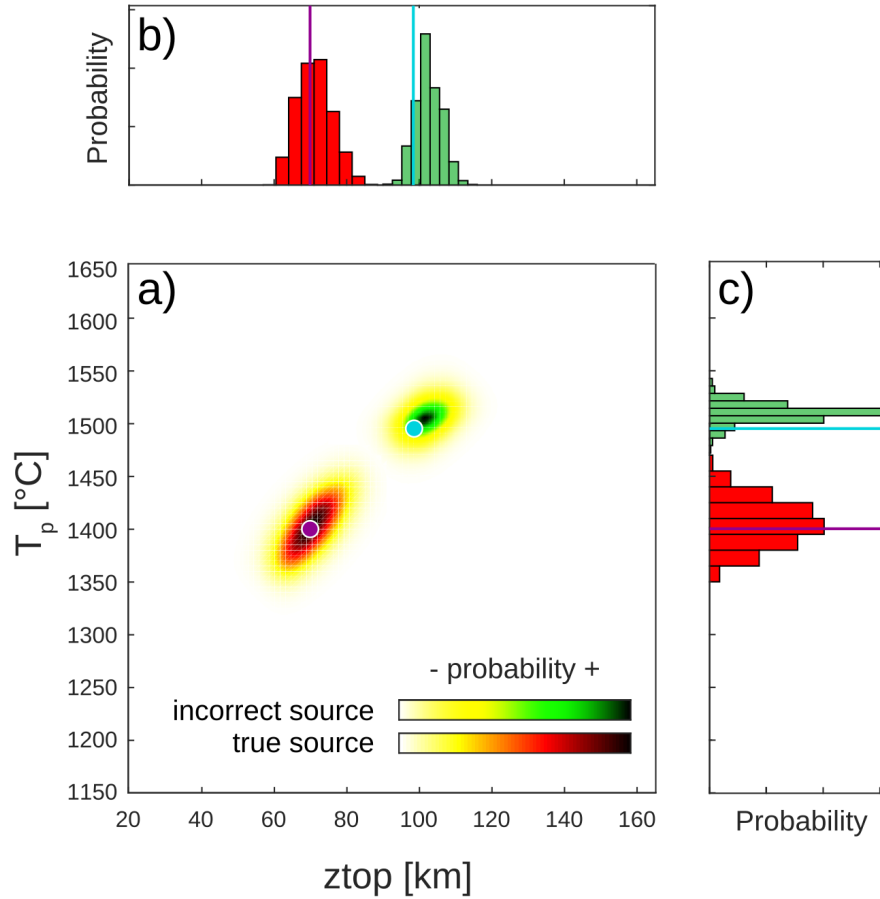
Figure 5: a) Joint posterior PDFs for Z_{top} and T_p given by two separate inversions. One used the true source composition (shown in red) whereas the other assumed an incorrect source composition obtained by adding 50% of a DMM component to the REEs and by depleting the Al_2O_3 and Na_2O contents by 0.7% and 0.1%, respectively (green). The purple dot represents the true solution ($Z_{top} = 70$ km and $T_p = 1400$ °C). The blue dot represents the solution from a deterministic inversion assuming the incorrect source composition. b) Marginal PDFs for Z_{top} for the two inversions. The purple line denotes the true solution. The blue line indicates the solution from the deterministic inversion assuming the incorrect source composition. c) Same as in b) but for T_p.

46
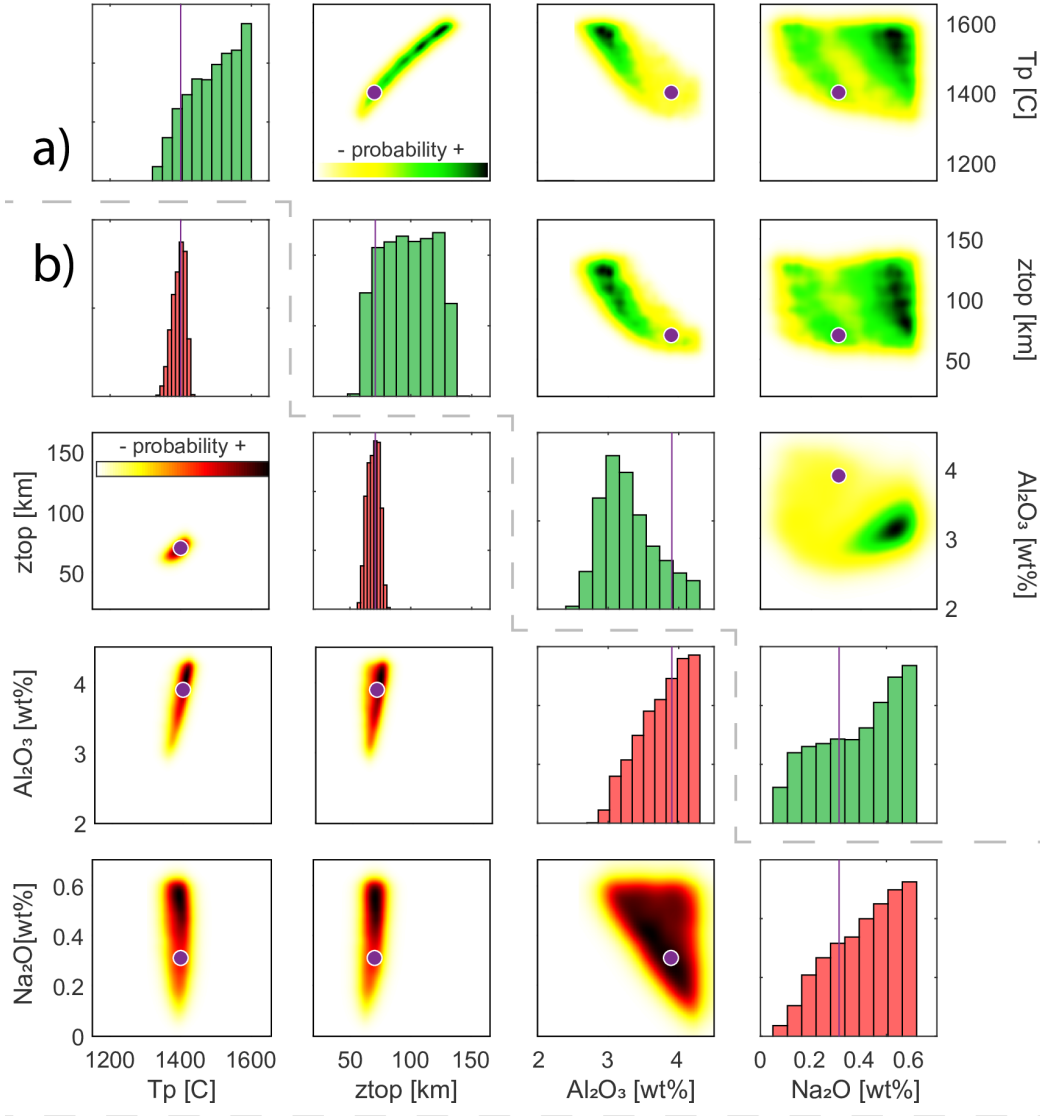
Figure 6: a) Marginal and joint posterior PDFs for the case where uncertainties in the major element composition of the source are explicitly considered in the inversion. Constant partition coefficients are assumed. Purple lines and dots denote the true values of the parameters. b) As in a) but adopting P-T-C-dependent partition coefficients. See text for details.
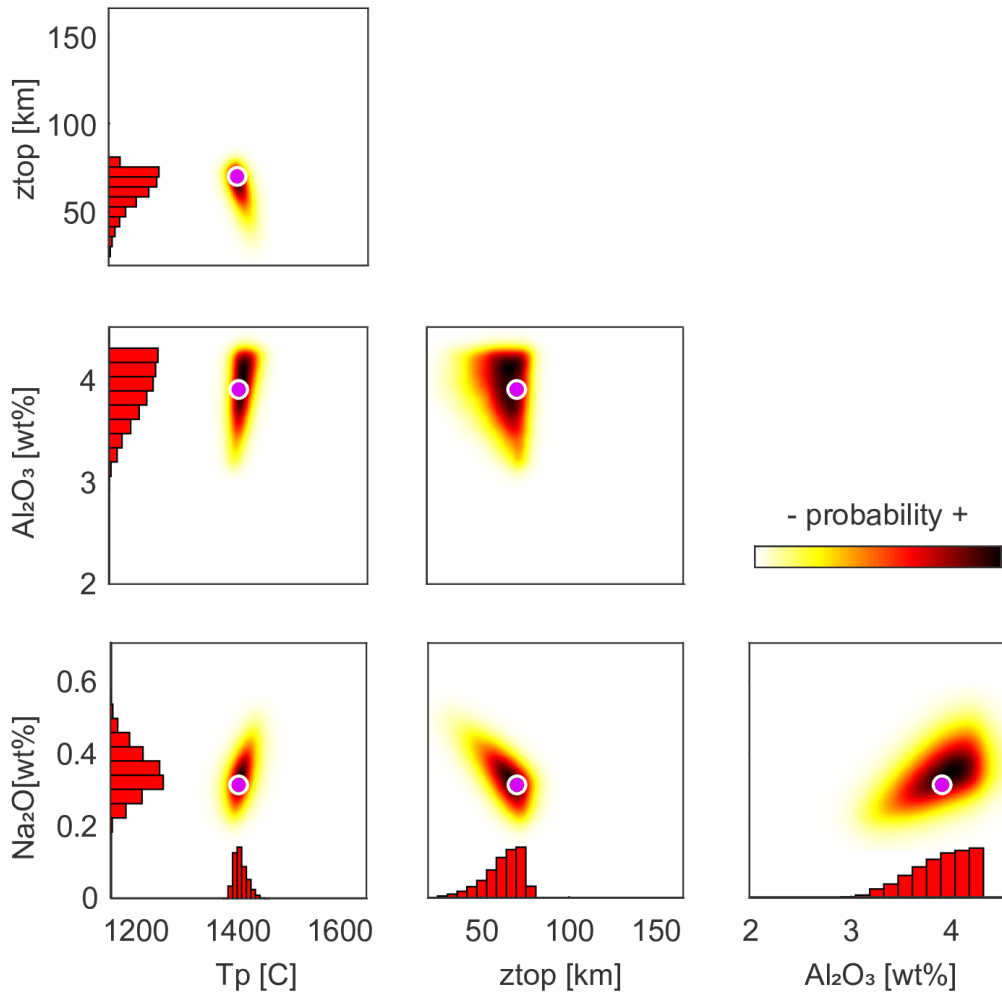
Figure 7: Joint and marginal posterior PDFs resulting from inverting major elements only. Pink circles indicate the true values of the parameters.

48
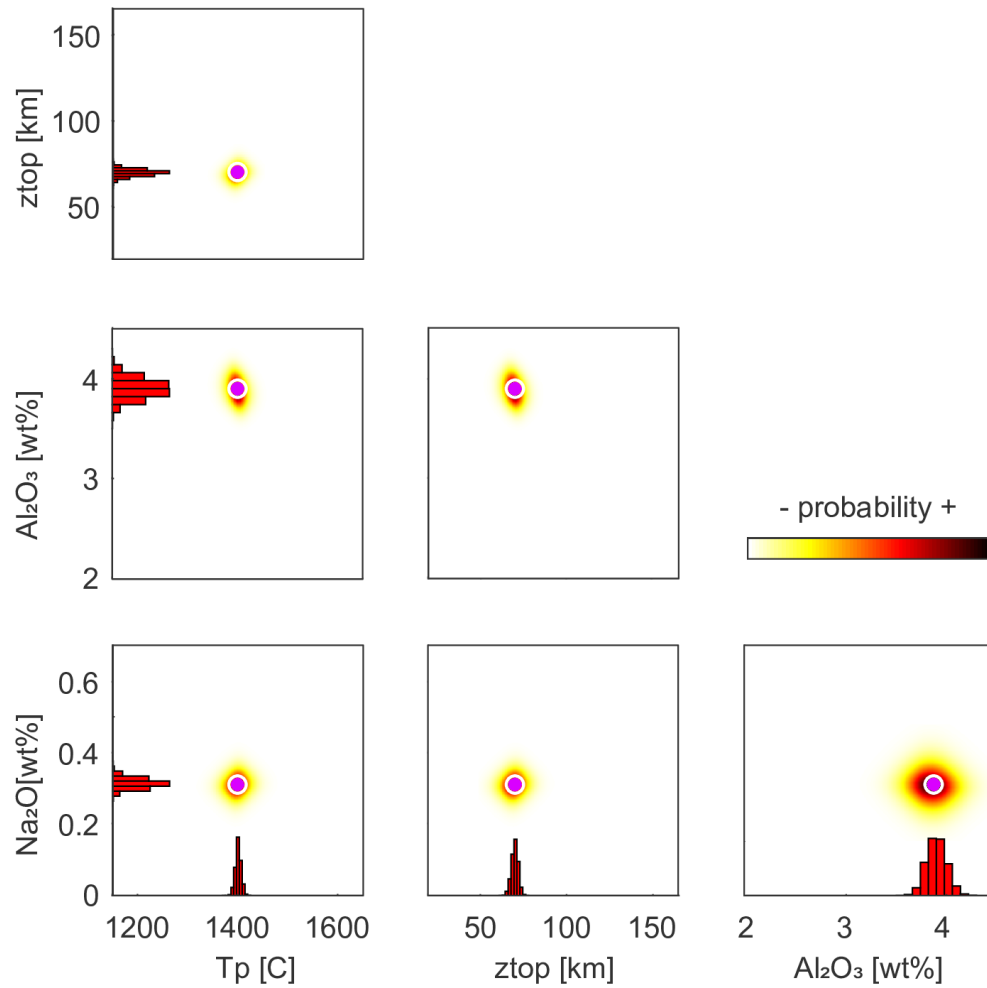
Figure 8: Joint and marginal posterior PDFs given by a joint inversion of REEs and major elements for Z_{top}, T_p and the Al_2O_3 and Na_2O contents of the source. Pink circles indicate the true values of the parameters.

Table 2: Model parameters and bounds of the uniform priors used in this study. The second and third columns corresponds to the reference values and prior ranges used in the inversion of synthetic data. The fourth column refers to the lower and upper bounds for REEs for the RGR example, which correspond to depleted MORB mantle (DMM) of Workman and Hart (2005) and primitive mantle (PM) of Palme and O'Neill (2014), respectively. Note that we interpret z_{top} to be the lithosphere-asthenosphere boundary.

Parameter	Value	Prior range - Synthetic	Prior range - RGR
z_{top} (km)	70	25–175	25–110
T_p (°C)	1400	1200–1600	1250–1520
Al_2O_3 (wt%)	3.9	2.1–4.3	3.1–4.2
Na_2O (wt%)	0.31	0.1–0.8	0.1–0.6
La (ppm)	0.683	0.0–1.0	0.192–0.700
Ce (ppm)	1.752	0.0–3.0	0.550–1.752
Pr (ppm)	0.265	0.0–1.0	0.107–0.265
Nd (ppm)	1.341	0.0–2.0	0.581–1.341
Sm (ppm)	0.434	0.0–1.0	0.239–0.434
Eu (ppm)	0.166	0.0–1.0	0.096–0.166
Gd (ppm)	0.585	0.0–1.0	0.358–0.585
Tb (ppm)	0.107	0.0–1.0	0.070–0.107
Dy (ppm)	0.724	0.0–1.5	0.505–0.730
Ho (ppm)	0.159	0.0–1.0	0.115–0.160
Er (ppm)	0.468	0.0–1.0	0.348–0.470
Yb (ppm)	0.477	0.0–1.0	0.365–0.480
Lu (ppm)	0.071	0.0–0.5	0.050–0.075
W_0 (cm/y)	5		
k_0 (m^{-1})	10^{-8}		
n	3		
μ_l (Pa s)	1		
R_j (s^{-1})	10^{-12}		
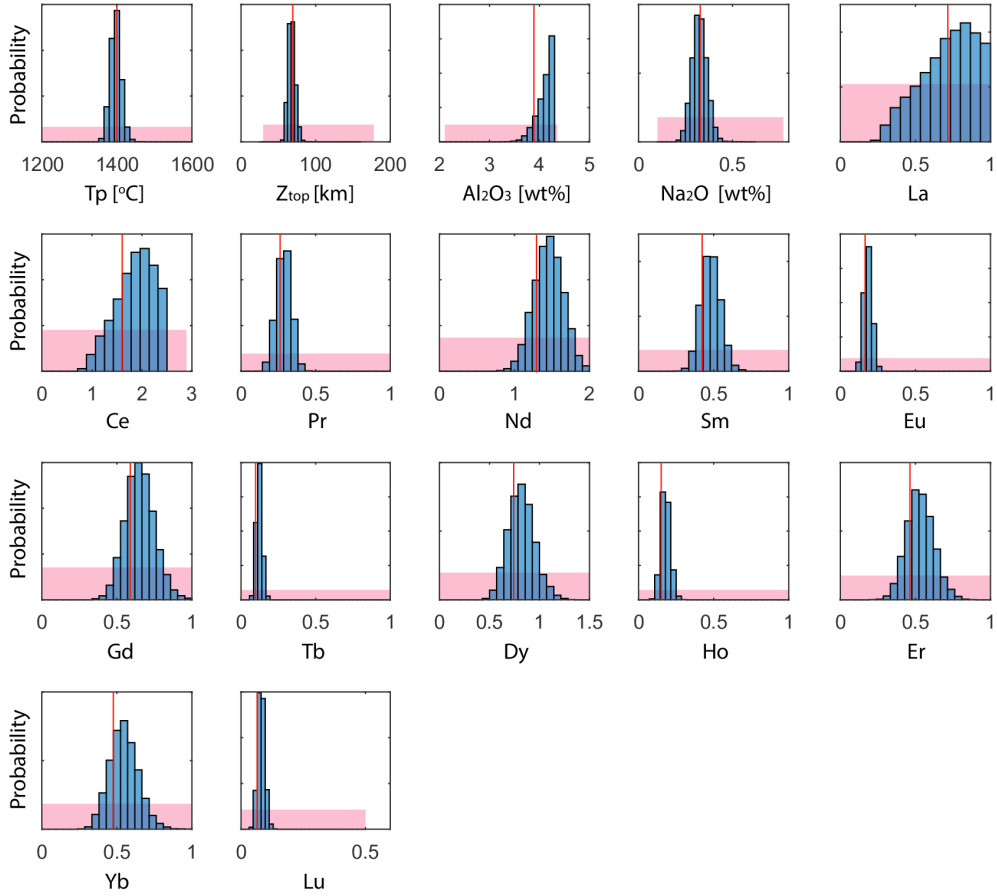
Figure 9: Marginal posterior PDFs for all seventeen model parameters given by a joint inversion of REEs and major elements. Pink boxes represent the (uniform) prior distributions used in the inversion. Red lines indicate the true values of the parameters. Joint distributions and correlations between parameters can be found in the electronic annex.

Table 3: Errors in computed melt composition due to uncertainties in the partition coefficients.

Element	Cpx ± 2STD	Grt ± 2STD	Error*
La	0.0490 ± 0.0245	0.001 ± 0.0005	9.9 %
Ce	0.0876 ± 0.0438	0.005 ± 0.0025	12.8 %
Pr	0.1260 ± 0.0630	0.014 ± 0.0070	18.9 %
Nd	0.1878 ± 0.0939	0.052 ± 0.0260	15.8 %
Sm	0.3083 ± 0.1542	0.250 ± 0.1250	17.0 %
Eu	0.3638 ± 0.1819	0.496 ± 0.2480	16.3 %
Gd	0.4169 ± 0.2085	0.848 ± 0.4240	16.7 %
Tb	0.4030 ± 0.2015	1.477 ± 0.7385	18.2 %
Dy	0.5034 ± 0.2517	2.200 ± 1.1000	19.7 %
Ho	0.5034 ± 0.2517	3.315 ± 1.6575	20.6 %
Er	0.5437 ± 0.2719	4.400 ± 2.2000	22.2 %
Yb	0.5453 ± 0.2727	6.600 ± 3.3000	24.2 %
Lu	0.5373 ± 0.2687	7.100 ± 3.5500	24.1 %

*These values refer to the error in computed melt composition as 1 STD.
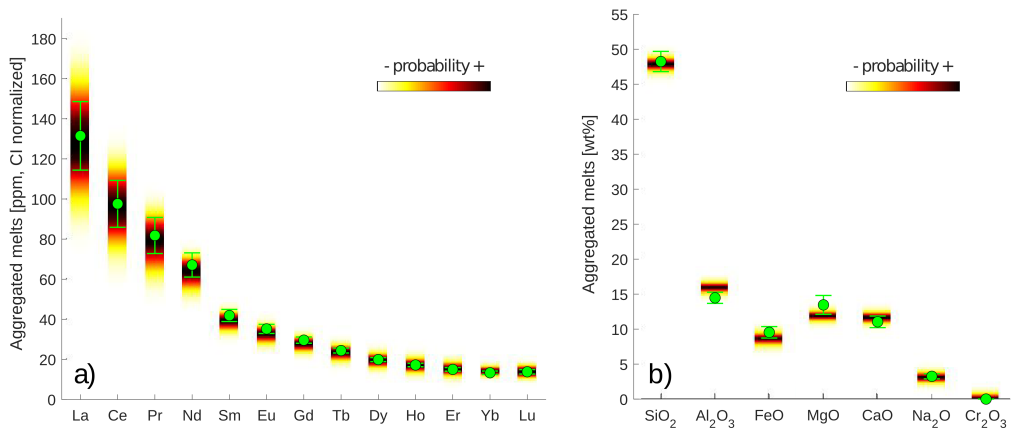
Figure 10: Data fits for the Rio Grande Rift samples from a joint inversion of REEs and major elements. a) Observed REE data (green dots with error bars) and corresponding marginal posterior PDFs. Note that in all cases, the means of the input data fall within one standard deviation of the marginal posterior. b) As in a) but for major elements (Cr_2O_3 was not considered in the inversion; a constant value of 0.2 wt% was assumed). Except for Al_2O_3 and MgO, input data and marginal posteriors overlap at the level of one standard deviation.
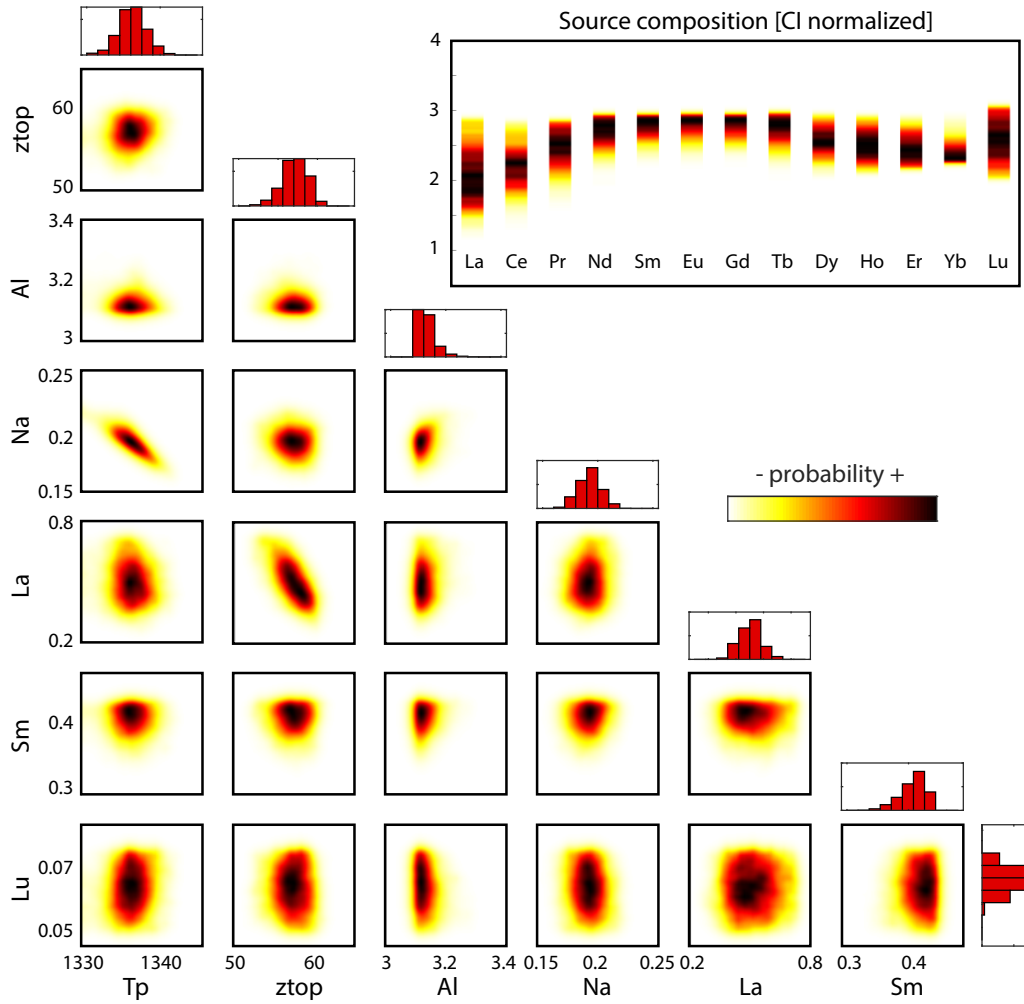
Figure 11: Joint and marginal posterior PDFs given by the joint inversion of the Rio Grande Rift samples. Marginal posterior PDFs for CI normalised REEs are shown in the upper right panel. Only a subset of the seventeen model parameters is shown here. A more complete depiction of the posterior PDF can be found in the electronic annex.

Appendix A. Two-phase, disequilibrium melting model

In section 2 we present the main equations for isentropic melting in a one-dimensional steady-state upwelling column. This appendix describes their derivation from a more general two-phase formalism. Table A.4 includes all the variables appearing in the formulation.

Appendix A.1. Mass conservation

Conservation of mass for a two-phase system composed of melt (l) and solid (s) phases reads

$$\frac{\partial (1 - \phi_l)\rho_s}{\partial t} + \nabla \cdot ((1 - \phi_l)\rho_s \mathbf{v}_s) = -\Gamma \tag{A.1}$$

$$\frac{\partial \phi_l \rho_l}{\partial t} + \nabla \cdot (\phi_l \rho_l \mathbf{v}_l) = \Gamma \tag{A.2}$$

where ϕ_l is the melt volume fraction, ρ is density, $\mathbf{v}$ is velocity, and Γ is the rate of mass exchange between phases (or simply, the melting rate).

We consider that the solid phase is comprised of several mineral grains j, each subject to a mass conservation equation of the type

$$\frac{\partial \phi_j \rho_j}{\partial t} + \nabla \cdot (\phi_j \rho_j \mathbf{v}_s) = -\Gamma_j \tag{A.3}$$

Equation A.3 implies that mineral grains move according to the solid velocity. Note also that Γ_j refers to the mass lost/gained by each mineral specie j; therefore we have that $\sum_j \Gamma_j = \Gamma$.

For a one-dimensional (depth-dependent only) steady-state case, Eqs. A.1, A.2 and A.3 can be integrated along z with the conditions $\phi_l(z = 0) = 0$ and $v_s(z = 0) = W_0$ at the bottom of the melting column ($z = 0$),

Table A.4: Main variables and definitions

Variable	Description	Unit
c	Composition	none
f	Melt mass fraction	nose
F	Degree of melting	nose
g	Gravity	m s^{-2}
D	Diffusion coefficient	m^2 s^{-1}
K	Partition coefficient	none
$k(\phi_l)$	Kozeny-Carman type permeability function	m^2
r	Radii of mineral grain	m
R	Diffusion-dependent exchange rate	m^2 s^{-1}
P	Pressure	Pa
S	Mass-transfer from instantaneous melt to isolated melt	Kg m^{-3} s^{-1}
T_p	Mantle potential temperature	C
w/W	Melt and solid velocities	m s^{-1}
z_{top}	Depth at which melting stops	m
Γ	Solid-to-fluid mass-transfer rate	Kg m^{-3} s^{-1}
μ	Shear viscosity	Pa s
ρ	Density	Kg m^{-3}
ϕ	Volume fraction	none

Index		
s, l	Solid, liquid	
eq, iso	Melts allowed to equilibrate and isolated	
b	Chemical component	
j	Thermodynamic phase or mineral phase	
0	Onset of melting	
ave	Averaged or pooled melts	

$$(1 - \phi_l)\rho_s W = \rho_s^0 W_0 - \int_0^h \Gamma dz \qquad (A.4)$$

$$\phi_l \rho_l w = \int_0^h \Gamma dz \qquad (A.5)$$

$$\phi_j \rho_j W = \phi_j^0 \rho_j^0 W_0 - \int_0^h \Gamma_j dz \qquad (A.6)$$

where W and w are the solid and liquid velocities, respectively, and h is the final depth of melting. We define the degree of melting $F(z)$ as the ratio between the total melt production flux and the flux of solid that enters the base of the column,

$$F(z) = \frac{\int_0^h \Gamma dz}{\rho_s^0 W_0} \qquad (A.7)$$

Similarly, for each mineral grain in the solid residue, we have

$$F_j(z) = \frac{\int_0^h \Gamma_j dz}{\rho_s^0 W_0} \qquad (A.8)$$

and mass conservation imposes that $\sum_j F_j = F$.

Combining Eqs. A.4, A.5 and A.6 with A.7 and A.8, we obtain the final mass-balance equations as functions of F,

$$(1 - \phi_l)\rho_s W = \rho_s^0 W_0(1 - F) \qquad (A.9)$$

$$\phi_l \rho_l w = \rho_s^0 W_0 F \qquad (A.10)$$

$$\phi_j \rho_j W = \rho_j^0 W_0 \left(\phi_j^0 - F_j \frac{\rho_s^0}{\rho_j^0} \right) \qquad (A.11)$$

Equations A.9 and A.10 need to be complemented with a third equation to obtain melt fraction (ϕ) and solid and melt velocities ($\mathbf{v}_s$ and $\mathbf{v}_l$) along

57

the melting column (for given $F(z)$, ρ_s and ρ_l). Here we use Darcy's law, where the velocity difference between solid and fluid is driven solely by the density difference. The segregation equation reads McKenzie (1984)

$$0 = \frac{d(W - w)}{\phi_l} + (1 - \phi_l)(\rho_s - \rho_l)\mathbf{g} \tag{A.12}$$

where d is a symmetric, rheology-dependent, interaction coefficient and modelled as (Bercovici et al., 2001)

$$d = \frac{\mu_s \mu_l \phi^2 (1 - \phi_l)^2}{\mu_l k (1 - \phi_l)\phi_l^2 + \mu_s k(\phi)(1 - \phi_l)^2} \tag{A.13}$$

where $k(\phi_l) = k_0(\phi_l)^n$ is the Kozeny–Carman-type permeability law relating permeability and porosity $k_0(\phi_l)$; n is a constant exponent. Here we take $n{=}3$.

Appendix A.2. Chemical transport in disequilibrium

Conservation of mass for a given chemical component (e.g. both major and trace chemical components) in the solid and liquid phases is given by

$$\frac{\partial(1 - \phi_l)\rho_s c_s^b}{\partial t} + \nabla \cdot \left((1 - \phi_l)\rho_s c_s^b \mathbf{v}_s\right) = -\Gamma^b \tag{A.14}$$

$$\frac{\partial \phi_l \rho_l c_l^b}{\partial t} + \nabla \cdot \left(\phi_l \rho_l c_l^b \mathbf{v}_l\right) = \Gamma^b \tag{A.15}$$

and since the solid phase is comprised of several mineral grains j, each is subjected to a mass conservation equation for its chemical composition, c_j^b,

$$\frac{\partial \phi_j \rho_j c_j^b}{\partial t} + \nabla \cdot \left(\phi_j \rho_j c_j^b \mathbf{v}_s\right) = -\Gamma_j^b \tag{A.16}$$

58

where $c_s^b = \frac{1}{\rho} \sum_j \phi_j \rho_j c_j^b$. Because the chemical-mass lost by the solid, Γ^b, is the aggregated contribution of each of its constituents, Γ_j^b, chemical-mass conservation imposes $\Gamma^b = \sum_j \Gamma_j^b$. Details on how to model Γ_j^b are provided in the next section.

To account for disequilibrium processes, we adapt the disequilibrium melting model by Oliveira et al. (2020), and assume that i) the solid does not interact chemically with all the melt that passes through it, and that ii) the chemical interaction between solid and liquid phases is controlled by diffusion of chemical species in the solid. Conceptually this corresponds to having two different melt reservoirs flowing through the solid: one in chemical isolation, and the other with diffusion-controlled chemical exchange with the surrounding solid. We refer to these reservoirs as *isolated* and *equilibrated* liquids, respectively. This approach is similar to two-porosity melting models (Iwamori, 1994; Liang and Parmentier, 2010), where melts are kept in chemical isolation inside channels.

Conservation of mass for chemical component b must be calculated for both liquid reservoirs, and the generalization of Eq. A.15 leads to,

$$\frac{\partial \phi_{eq} \rho_l c_{eq}^b}{\partial t} + \nabla \cdot \left(\phi_{eq} \rho_l c_{eq}^b \mathbf{v}_l \right) = \Gamma^b - c_{eq}^b S \tag{A.17}$$

$$\frac{\partial \phi_{iso} \rho_l c_{iso}^b}{\partial t} + \nabla \cdot \left(\phi_{iso} \rho_l c_{iso}^b \mathbf{v}_l \right) = c_{eq}^b S \tag{A.18}$$

where ϕ_{eq} and ϕ_{iso} are the volume liquid fractions allowed to equilibrate and that in chemical isolation, respectively. Because of mass-balance constraints $\phi_{eq} + \phi_{iso} = \phi_l$. S is the rate of mass exchange between both liquid reservoirs, and $c_{eq}^b S$ is the mass of chemical component b associated to this mass transfer.

59

Similarly, mass conservation for the equilibrated and isolated liquid reads,

$$\frac{\partial \phi_{eq}\rho_l}{\partial t} + \nabla \cdot (\phi_{eq}\rho_l \mathbf{v}_l) = \Gamma - S \qquad (A.19)$$

$$\frac{\partial \phi_{iso}\rho_l}{\partial t} + \nabla \cdot (\phi_{iso}\rho_l \mathbf{v}_l) = S \qquad (A.20)$$

For one-dimensional steady-state melting columns, Eqs. A.14, A.17, A.16, A.18, A.19 and A.20 can be rewritten as

$$(1 - \phi_l)\rho_s W \frac{dc_s^b}{dz} = -\Gamma^b + c_s^b \Gamma \qquad (A.21)$$

$$\phi_j \rho_j W \frac{dc_j^b}{dz} = -\Gamma_j^b + c_j^b \Gamma_j \qquad (A.22)$$

$$\phi_{eq}\rho_l w \frac{dc_{eq}^b}{dz} = \Gamma^b - c_l^b \Gamma \qquad (A.23)$$

$$\phi_{iso}\rho_l w \frac{dc_{iso}^b}{dz} = \left(c_{eq}^b - c_{iso}^b\right) S \qquad (A.24)$$

$$\phi_{eq}\rho_l w = \rho_s^0 W_0 F - \int_0^h S dz \qquad (A.25)$$

$$\phi_{iso}\rho_l w = \int_0^h S dz \qquad (A.26)$$

Appendix A.2.1. Γ_j^b

To account for the chemical mass exchange between solid and the equilibrated liquid phase, we split Γ_j^b into two parts (Rudge et al., 2011),

$$\Gamma_j^b = c_{\Gamma,j}^b \Gamma_j + J_j^b \qquad (A.27)$$

In Eq. A.27 we explicitly consider that chemical-mass transfer between solid and equilibrated liquid phases occurs as a consequence of two distinct processes: one with phase change (i.e. production of local melt, $c_{\Gamma,j}^b \Gamma_j$, where

60

$c^b_{\Gamma,j}$ represents the mass concentrations of the melt produced from mineral phase j), and another without phase change (i.e. because of diffusive fluxes, J^b_j). There is no unique choice for the pair $c^b_{\Gamma,j}$ and J^b_j.

A possible choice for $c^b_{\Gamma,j}$ is to consider that the newly produced melt is always in local equilibrium with the solid (i.e. an instantaneous fractional melt),

$$c^b_{\Gamma,j} = c^b_j/K^b_j \tag{A.28}$$

where K^b_j is the usual partition coefficient.

Alternatively, one could fix the solid composition as melting proceeds (i.e. solid invariant melting) which leads to,

$$c^b_{\Gamma,j} = c^b_j \tag{A.29}$$

Equations A.28 and A.29 represent two natural choices for the liquid composition associated with melting based on the solid composition. There is plenty of scope for further exploration of these laws.

For J^b_j, we use linear kinetics to approximate mineral–melt finite exchange that arises from diffusion in minerals and/or dissolution–precipitation,

$$J^b_j = \phi_j \rho_j R^b_j \left(c^b_j - K^b_j c^b_{eq} \right) \tag{A.30}$$

where R^b_j is the exchange rate constant for the chemical component of interest between mineral j and the melt. As mentioned above, we consider that solid diffusion (i.e. intra-diffusion) is the limiting factor controlling the exchange of chemical components between mineral grains and melt. Thus, the exchange

rate R_j^b is proportional to diffusion coefficient of the element of interest in the mineral (D_j^b), and inversely proportional to the grain size r_j

$$R_j^b = \frac{3\beta D_j^b}{r_j^2}, \tag{A.31}$$

where $\beta = 5$ is a geometric factor describing diffusion in a plane sheet, cylinder or sphere (e.g., Navon and Stolper (1987); Bodinier et al. (1990)). Hence fast diffusivities or small grain sizes will tend to equilibrate the system (i.e. $c_j^b = K_j^b c_{eq}^b$).

Appendix A.3. Final considerations and summary of governing equations

In this work we consider a one-dimensional upwelling column under steady-state conditions. The system is comprised of an aggregate of mineral phases j (i.e. an aggregate of ol, cpx, opx, grt, sp and plg phases forming the solid phase) and two melt reservoirs, which we refer to as *equilibrated* and *isolated* liquid. The former interacts chemically with the surrounding solid, whereas the later is kept in chemical isolation. For the purpose of this work, we assume that all the newly formed melts are kept in chemical isolation, which implies that all the volume of liquid flowing through the solid residue corresponds to the *isolated* liquid reservoir, i.e. $\phi_l = \phi_{iso}$ and $\phi_{eq} = 0$. Therefore, the *equilibrated* melts correspond to the *instantaneous* melts formed during partial melting, which are pooled with the isolated melts upwelling from beneath as soon as they are formed, i.e. $S = \Gamma$. Note that depending on the diffusivity of chemical component b in the solid phase, instantaneous melts may or may not be in complete chemical equilibrium with the surrounding solid.

62

Following these considerations, the final systems of equations governing the forward model in our inversions are

Mass conservation in residual solid, s:

$$(1 - \phi_l)\rho_s W = \rho_s^0 W_0 (1 - F) \tag{A.32}$$

Mass conservation in liquid, l:

$$\phi_l \rho_l w = \rho_s^0 W_0 F \tag{A.33}$$

Mass conservation in mineral grains, j

$$\phi_j \rho_j W = \rho_j^0 W_0 \left(\phi_j^0 - F_j \frac{\rho_s^0}{\rho_j^0} \right) \tag{A.34}$$

Chemical-mass conservation in residual solid, s:

$$(1 - \phi_l)\rho_s W \frac{dc_s^b}{dz} = \sum_j \Gamma_j \left(c_j^b - c_{\Gamma,j}^b \right) - \sum_j \phi_j \rho_j R_j^b \left(c_j^b - K_j^b c_l^b \right) \tag{A.35}$$

Chemical-mass conservation in isolated melt, iso:

$$\phi_l \rho_l w \frac{dc_{iso}^b}{dz} = \left(c_{inst}^b - c_{iso}^b \right) \Gamma \tag{A.36}$$

where the instantaneous melt composition c_{inst}^b reads

$$c_{inst}^b = \frac{\sum_j \Gamma_j c_{\Gamma,j}^b + \sum_j \phi_j \rho_j R_j^b c_j^b}{\sum_j \Gamma_j + \sum_j \phi_j \rho_j R_j^b K_j^b} \tag{A.37}$$

Chemical-mass conservation in mineral grains, j:

$$\phi_j \rho_j W \frac{dc_j^b}{dz} = \Gamma_j \left(c_j^b - c_{\Gamma,j}^b \right) - \phi_j \rho_j R_j^b \left(c_j^b - K_j^b c_{inst}^b \right) \tag{A.38}$$

63

Melt segregation:

$$0 = \frac{\mu_l}{k_0 \phi^{n-1}}(W - w) + (1 - \phi_l)(\rho_s - \rho_l)\mathbf{g} \qquad (A.39)$$

Equations A.32–A.39 represent a set of eight equations for eight unknowns, namely liquid fraction (ϕ_l), mineral phase fractions (ϕ_j), chemical composition of residual solid, liquids and mineral grains (c_s^b, c_{inst}^b, c_{iso}^b and c_j^b, respectively) and solid and melt velocities (W and w). This set of equations is solved for given sets of material properties (e.g. ρ, μ) and closure terms (e.g. Γ, Γ^b).

Appendix B. Numerical solution of the forward problem

The computation of the forward problem is divided into four parts.

- First, given a a set of model parameters (i.e. T_p, z_{top}, Al_2O_3 and Na_2O) we compute the melting and chemistry function for major element composition as described in Section 2.2 using Perple_X. In order to speed up this step, we make use of lookup tables, which had previously been computed in an $offline$ stage. These lookup tables contain individual isentropic decompression melting models as a function of model parameters, which have been discretised over a numerical grid. Preliminary tests informed our discretization choice (to keep the numerical error well below typical errors in the data). We use 5 °C, 1 km, 0.2 wt%, and 0.05 wt% for T_p, z_{top}, Al_2O3 and Na_2O, respectively. From these lookup tables we extract the information of six different melting columns corresponding to the values of T_p-Al_2O_3-Na_2O that fall closest to trial set of parameters (i.e. the 6 vertices of the closest prism

within the used T_p-Al_2O_3-Na_2O discretization space). For each of these 8 melting columns we extract i) the mineral phase distributions ϕ_j and their properties, ii) fluid and solid major element compositions c_{inst}, iii) degree of melting F, and iv) temperature profile along the melting column (i.e. from the onset of melting all the way to z_{top}).

- Second, we obtain melt volume phi_l and melt and solid ascending velocities W and w by jointly solving both mass and melt segregation equations for each melting column.

- Third, we obtain the trace element composition of both solid and liquid phases along the melting columns by solving the chemistry function for each trace element as a function of their ascending velocities, volume fractions, partition coefficients, diffusivities and other physical properties. This is done using a standard finite difference approach.

- Last, we compute the averaged major and trace element concentration of the pooled magma using the mixing function of Eq. 14 for each melting column, and then interpolating the result for the given set of model parameters.

References

Afonso, J., Fullea, J., Griffin, W., Yang, Y., Jones, A., D. Connolly, J., O'Reilly, S., 2013a. 3-d multiobservable probabilistic inversion for the compositional and thermal structure of the lithosphere and upper mantle. i: A priori petrological information and geophysical observables. Journal of Geophysical Research: Solid Earth 118, 2586–2617.

Afonso, J.C., Fullea, J., Yang, Y., Connolly, J., Jones, A., 2013b. 3-d multi-observable probabilistic inversion for the compositional and thermal structure of the lithosphere and upper mantle. ii: General methodology and resolution analysis. Journal of Geophysical Research: Solid Earth 118, 1650–1676.

Afonso, J.C., Rawlinson, N., Yang, Y., Schutt, D.L., Jones, A.G., Fullea, J., Griffin, W.L., 2016. 3-D multiobservable probabilistic inversion for the compositional and thermal structure of the lithosphere and upper mantle: III. Thermochemical tomography in the Western-Central U.S. Journal of Geophysical Research: Solid Earth 121, 7337–7370. doi:10.1002/2016JB013049.

Afonso, J.C., Salajegheh, F., Szwillus, W., Ebbing, J., Gaina, C., 2019. A global reference model of the lithosphere and upper mantle from joint inversion and analysis of multiple data sets. Geophysical Journal International 217, 1602–1628.

Albarède, F., 1983. Inversion of batch melting equations and the trace element pattern of the mantle. Journal of Geophysical Research: Solid Earth 88, 10573–10583.

Asimow, P.D., 2001. Calculation of Peridotite Partial Melting from Thermodynamic Models of Minerals and Melts, IV. Adiabatic Decompression and the Composition and Mean Properties of Mid-ocean Ridge Basalts. Journal of Petrology 42, 963–998. doi:10.1093/petrology/42.5.963.

Asimow, P.D., 2002. Steady-state Mantle-Melt Interactions in One Dimen-

sion: II. Thermal Interactions and Irreversible Terms. Journal of Petrology 43, 1707–1724. doi:10.1093/petrology/43.9.1707.

Asimow, P.D., Hirschmann, M., Stolper, E., 1997. An analysis of variations in isentropic melt productivity. Philosophical Transactions of the Royal Society of London. Series A: Mathematical, Physical and Engineering Sciences 355, 255–281.

Asimow, P.D., Stolper, E.M., 1999. Steady-state mantle-melt interactions in one dimension: I. Equilibrium transport and melt focusing. Journal of Petrology doi:10.1093/petroj/40.3.475.

Ayyub, B.M., Klir, G.J., 2006. Uncertainty modeling and analysis in engineering and the sciences. CRC Press.

Bercovici, D., Ricard, Y., Schubert, G., 2001. A two-phase model for compaction and damage: 1. general theory. Journal of Geophysical Research: Solid Earth 106, 8887–8906.

Bodinier, J., Vasseur, G., Vernieres, J., Dupuy, C., Fabries, J., 1990. Mechanisms of mantle metasomatism: geochemical evidence from the lherz orogenic peridotite. Journal of Petrology 31, 597–628.

Brooks, S., Gelman, A., Jones, G., Meng, X.L., 2011. Handbook of markov chain monte carlo. CRC press.

Brown, E.L., Lesher, C.E., 2016. Reebox pro: A forward model simulating melting of thermally and lithologically variable upwelling mantle. Geochemistry, Geophysics, Geosystems 17, 3929–3968.

Brown, E.L., Petersen, K.D., Lesher, C.E., 2020. Markov chain monte carlo inversion of mantle temperature and source composition, with application to reykjanes peninsula, iceland. Earth and Planetary Science Letters 532, 116007.

Christiansen, R.L., Lipman, P.W., 1972. Cenozoic Volcanism and Plate-Tectonic Evolution of the Western United States. II. Late Cenozoic. Philosophical Transactions of the Royal Society of London A: Mathematical, Physical and Engineering Sciences 271, 249–284. doi:10.1098/rsta.1972.0009.

Connolly, J., 2009. The geodynamic equation of state: what and how. Geochemistry, Geophysics, Geosystems 10.

Danyushevsky, L.V., Plechov, P., 2011. Petrolog3: Integrated software for modeling crystallization processes. Geochemistry, Geophysics, Geosystems 12, Q07021. doi:10.1029/2011GC003516.

Feigenson, M.D., Patino, L.C., Carr, M.J., 1996. Constraints on partial melting imposed by rare earth element variations in mauna kea basalts. Journal of Geophysical Research: Solid Earth 101, 11815–11829.

Fitton, J.G., James, D., Leeman, W.P., 1991. Basic magmatism associated with Late Cenozoic extension in the western United States: Compositional variations in space and time. Journal of Geophysical Research: Solid Earth 96, 13693–13711. doi:10.1029/91JB00372.

Gast, P.W., 1968. Trace element fractionation and the origin of tholeiitic and alkaline magma types. Geochimica et Cosmochimica Acta 32, 1057–1086.

68

Ghiorso, M.S., Hirschmann, M.M., Reiners, P.W., Kress, V.C., 2002. The pmelts: A revision of melts for improved calculation of phase relations and major element partitioning related to partial melting of the mantle to 3 gpa. Geochemistry, Geophysics, Geosystems 3, 1–35.

Gürlebeck, K., Legatiuk, D., Nilsson, H., Smarsly, K., 2020. Conceptual modelling: Towards detecting modelling errors in engineering applications. Mathematical Methods in the Applied Sciences 43, 1243–1252.

Haario, H., Saksman, E., Tamminen, J., et al., 2001. An adaptive metropolis algorithm. Bernoulli 7, 223–242.

Herzberg, C., 2004. Partial crystallization of mid-ocean ridge basalts in the crust and mantle. Journal of Petrology 45, 2389–2405.

Herzberg, C., O'Hara, M., 2002. Plume-associated ultramafic magmas of phanerozoic age. Journal of Petrology 43, 1857–1883.

Hofmann, A., Feigenson, M., 1983. Case studies on the origin of basalt. Contributions to Mineralogy and Petrology 84, 382–389.

Holland, T.J., Green, E.C., Powell, R., 2018. Melting of peridotites through to granites: a simple thermodynamic model in the system kncfmashtocr. Journal of Petrology 59, 881–900.

Hopper, E., Fischer, K.M., 2018. The changing face of the lithosphere-asthenosphere boundary: Imaging continental scale patterns in upper mantle structure across the contiguous U.S. with Sp converted waves. Geochemistry, Geophysics, Geosystems 19, 2593–2614. doi:10.1029/2018GC007476.

Ito, G., Mahoney, J.J., 2005. Flow and melting of a heterogeneous mantle: 1. method and importance to the geochemistry of ocean island and mid-ocean ridge basalts. Earth and Planetary Science Letters 230, 29–46.

Iwamori, H., 1993. Dynamic disequilibrium melting model with porous flow and diffusion-controlled chemical equilibration. Earth and planetary science letters 114, 301–313.

Iwamori, H., 1994. 238u-230th-226ra and 235u-231pa disequilibria produced by mantle melting with porous and channel flows. Earth and Planetary Science Letters 125, 1–16.

Jennings, E.S., Holland, T.J., 2015. A simple thermodynamic model for melting of peridotite in the system ncfmasocr. Journal of Petrology 56, 869–892.

Kaipio, J.P., Somersalo, E., 2005. Statistical inversion theory. Statistical and computational inverse problems , 49–114.

Katz, R.F., Spiegelman, M., Langmuir, C.H., 2003. A new parameterization of hydrous mantle melting. Geochemistry, Geophysics, Geosystems 4.

Keller, T., Katz, R.F., 2016. The role of volatiles in reactive melt transport in the asthenosphere. Journal of Petrology 57, 1073–1108. doi:10.1093/petrology/egw030.

Keller, T., Katz, R.F., Hirschmann, M.M., 2017. Volatiles beneath mid-ocean ridges: Deep melting, channelised transport, focusing, and metasomatism. Earth and Planetary Science Letters 464, 55–68. doi:10.1016/j.epsl.2017.02.006.

Kent, A.J., 2008. Melt inclusions in basaltic and related volcanic rocks. Reviews in Mineralogy and Geochemistry 69, 273–331.

Khan, A., Zunino, A., Deschamps, F., 2013. Upper mantle compositional variations and discontinuity topography imaged beneath Australia from Bayesian inversion of surface-wave phase velocities and thermochemical modeling. Journal of Geophysical Research: Solid Earth 118, 5285–5306. doi:10.1002/jgrb.50304.

Kimura, J.I., 2017. Modeling chemical geodynamics of subduction zones using the Arc Basalt Simulator version 5. Geosphere 13, 992–1025. doi:10.1130/GES01468.S2.

Klein, E.M., Langmuir, C.H., 1987. Global correlations of ocean ridge basalt chemistry with axial depth and crustal thickness. Journal of Geophysical Research: Solid Earth 92, 8089–8115.

Klöcking, M., White, N.J., Maclennan, J., McKenzie, D., Fitton, J.G., 2018. Quantitative Relationships Between Basalt Geochemistry, Shear Wave Velocity, and Asthenospheric Temperature Beneath Western North America. Geochemistry, Geophysics, Geosystems 19, 3376–3404. doi:10.1029/2018GC007559.

Korenaga, J., Kelemen, P.B., 2000. Major element heterogeneity in the mantle source of the North Atlantic igneous province. Earth and Planetary Science Letters 184, 251–268. doi:10.1016/S0012-821X(00)00308-3.

Langmuir, C.H., Klein, E.M., Plank, T., 1992. Petrological systematics of

71

1274   mid-ocean ridge basalts: Constraints on melt generation beneath ocean
1275   ridges. Mantle flow and melt generation at mid-ocean ridges 71, 183–280.

1276   Liang, Y., Liu, B., 2016. Simple models for disequilibrium fractional melting
1277   and batch melting with application to ree fractionation in abyssal peri-
1278   dotites. Geochimica et Cosmochimica Acta 173, 181–197.

1279   Liang, Y., Parmentier, E.M., 2010. A two-porosity double lithology model for
1280   partial melting, melt transport and melt–rock reaction in the mantle: Mass
1281   conservation equations and trace element transport. Journal of Petrology
1282   51, 125–152.

1283   Liu, B., Liang, Y., 2017. An introduction of markov chain monte carlo
1284   method to geochemical inverse problems: Reading melting parameters
1285   from ree abundances in abyssal peridotites. Geochimica et Cosmochim-
1286   ica Acta 203, 216–234.

1287   Liu, J.Q., Chen, L.H., Zeng, G., Wang, X.J., Zhong, Y., Yu, X., 2016. Litho-
1288   spheric thickness controlled compositional variations in potassic basalts of
1289   northeast china by melt-rock interactions. Geophysical Research Letters
1290   43, 2582–2589.

1291   Liu, J.S., 2008. Monte Carlo Strategies in Scientific Comput-
1292   ing. Springer Series in Statistics, Springer New York, New York,
1293   NY. URL: http://link.springer.com/10.1007/978-0-387-76371-2,
1294   doi:10.1007/978-0-387-76371-2.

1295   Mallik, A., Dasgupta, R., 2012. Reaction between morb-eclogite derived

melts and fertile peridotite and generation of ocean island basalts. Earth and Planetary Science Letters 329, 97–108.

McKenzie, D., 1984. The generation and compaction of partially molten rock. Journal of petrology 25, 713–765.

McKenzie, D., O'Nions, R., 1991. Partial melt distributions from inversion of rare earth element concentrations. Journal of Petrology 32, 1021–1091.

Michard, A., Albarède, F., 1986. The ree content of some hydrothermal fluids. Chemical Geology 55, 51–60.

Miesch, A.T., 1967. Theory of error in geochemical data. Technical Report. United States Geological Survey, Professional Paper 574-A.

Minster, J., Allègre, C., 1978. Systematic use of trace elements in igneous processes. Contributions to Mineralogy and Petrology 68, 37–52.

Morgan, J.P., 2001. Thermodynamics of pressure release melting of a veined plum pudding mantle. Geochemistry, Geophysics, Geosystems 2.

Navon, O., Stolper, E., 1987. Geochemical consequences of melt percolation: the upper mantle as a chromatographic column. The Journal of Geology 95, 285–307.

Niu, Y., Batiza, R., 1991. An empirical method for calculating melt compositions produced beneath mid-ocean ridges: Application for axis and off-axis (seamounts) melting. Journal of Geophysical Research: Solid Earth 96, 21753–21777.

Oliveira, B., Afonso, J.C., Tilhac, R., 2020. A disequilibrium reactive transport model for mantle magmatism. Journal of Petrology , egaa067doi:10.1093/petrology/egaa067.

Oliveira, B., Afonso, J.C., Zlotnik, S., Diez, P., 2017. Numerical modelling of multiphase multicomponent reactive transport in the earth's interior. Geophysical Journal International 212, 345–388.

Oliveira, B.n., Afonso, J.C., Klöcking, M., 2021. Software from "Melting conditions and mantle source composition from probabilistic joint inversion of major and rare earth element concentrations". URL: https://doi.org/10.5281/zenodo.5163125, doi:10.5281/zenodo.5163125.

Palme, H., O'Neill, H., 2014. Cosmochemical Estimates of Mantle Composition, in: Treatise on Geochemistry: Second Edition. Elsevier Inc.. volume 3, pp. 1–39. doi:10.1016/B978-0-08-095975-7.00201-1.

Plank, T., Langmuir, C.H., 1992. Effects of the melting regime on the composition of the oceanic crust. Journal of Geophysical Research: Solid Earth 97, 19749–19770.

Ribe, N.M., 1985. The deformation and compaction of partial molten zones. Geophysical Journal of the Royal Astronomical Society 83, 487–501. doi:10.1111/j.1365-246X.1985.tb06499.x.

Richter, F.M., 1986. Simple models for trace element fractionation during melt segregation. Earth and Planetary Science Letters 77, 333–344.

Rudge, J.F., Bercovici, D., Spiegelman, M., 2011. Disequilibrium melting of a two phase multicomponent mantle. Geophysical Journal International 184, 699–718.

Smith, P.M., Asimow, P.D., 2005. Adiabat_1ph: A new public front-end to the melts, pmelts, and phmelts models. Geochemistry, Geophysics, Geosystems 6.

Smith, R.C., 2013. Uncertainty quantification: theory, implementation, and applications. volume 12. SIAM.

Stolper, E.M., Shorttle, O., Antoshechkina, P.M., Asimow, P.D., 2020. The effects of solid-solid phase equilibria on the oxygen fugacity of the upper mantle. American Mineralogist 105, 1445–1471.

Tarantola, A., 2005. Inverse problem theory and methods for model parameter estimation. SIAM.

Thompson, R.N., Ottley, C.J., Smith, P.M., Pearson, D.G., Dickin, A.P., Morrison, M.A., Leat, P.T., Gibson, S.A., 2005. Source of the quaternary alkalic basalts, picrites and basanites of the Potrillo Volcanic Field, New Mexico, USA: Lithosphere or convecting mantle? Journal of Petrology 46, 1603–1643. doi:10.1093/petrology/egi028.

Tirone, M., Ganguly, J., Morgan, J., 2009. Modeling petrological geodynamics in the earth's mantle. Geochemistry, Geophysics, Geosystems 10.

Tweto, O., 1979. The Rio Grande rift system in Colorado, in: Rio Grande Rift: Tectonics and Magmatism (ed R. E. Riecker), American Geophysical Union, Washington, D. C.. volume 14, pp. 33–56.

Van Westrenen, W., Blundy, J.D., Wood, B.J., 2001. High field strength element/rare earth element fractionation during partial melting in the presence of garnet: Implications for identification of mantle heterogeneities. Geochemistry, Geophysics, Geosystems 2.

Wood, B.J., Blundy, J.D., 1997. A predictive model for rare earth element partitioning between clinopyroxene and anhydrous silicate melt. Contributions to Mineralogy and Petrology 129, 166–181.

Wood, B.J., Blundy, J.D., 2014. Trace Element Partitioning: The Influences of Ionic Radius, Cation Charge, Pressure, and Temperature, in: Treatise on Geochemistry: Second Edition. doi:10.1016/B978-0-08-095975-7.00209-6.

Workman, R.K., Hart, S.R., 2005. Major and trace element composition of the depleted morb mantle (dmm). Earth and Planetary Science Letters 231, 53–72.

Yang, Z.F., Li, J., Jiang, Q.B., Xu, F., Guo, S.Y., Li, Y., Zhang, J., 2019. Using major element logratios to recognize compositional patterns of basalt: Implications for source lithological and compositional heterogeneities. Journal of Geophysical Research: Solid Earth 124, 3458–3490. doi:https://doi.org/10.1029/2018JB016145.

Zou, H., 1997. Inversion of partial melting through residual peridotites or clinopyroxenes. Geochimica et cosmochimica acta 61, 4571–4582.